

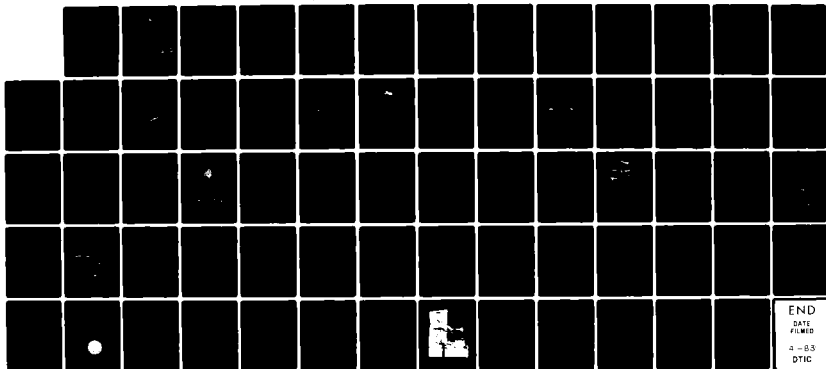
AD-A126 261

V/STOL FOUNTAIN FORCE COEFFICIENT(U) MCDONNELL AIRCRAFT 1/1  
CO ST LOUIS MO L W GLAZE ET AL. JAN 83 NADC-81106-60  
N62269-81-C-0717

UNCLASSIFIED

F/G 1/3

NL



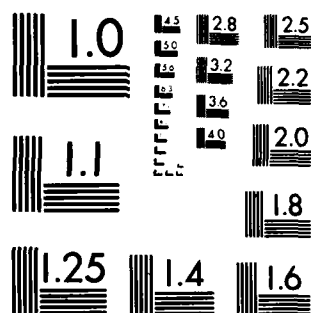
END

DATE

FILMED

4-83

DTIC



MICROCOPY RESOLUTION TEST CHART  
NATIONAL BUREAU OF STANDARDS-1963-A

(12)



ADA 126261

# V/STOL FOUNTAIN FORCE COEFFICIENT

JANUARY 1983

L.W. GLAZE  
D.R. BRISTOW  
D.R. KOTANSKY

MCDONNELL AIRCRAFT COMPANY  
MCDONNELL DOUGLAS CORPORATION  
P.O. BOX 516  
ST. LOUIS, MISSOURI 63166

DTIC  
ELECTE  
APR 1 1983  
S A

APPROVED FOR PUBLIC RELEASE; DISTRIBUTION UNLIMITED

PREPARED FOR  
UNITED STATES NAVY  
NAVAL AIR DEVELOPMENT CENTER  
WARMINSTER, PA 18974

DTIC FILE COPY

83 04 01 C18

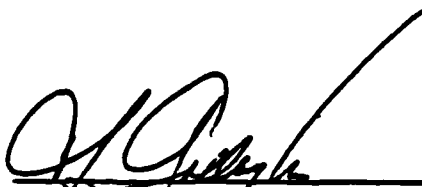
## NOTICES

**REPORT NUMBERING SYSTEM** - The numbering of technical project reports issued by the Naval Air Development Center is arranged for specific identification purposes. Each number consists of the Center acronym, the calendar year in which the number was assigned, the sequence number of the report within the specific calendar year, and the official 2-digit correspondence code of the Command Office or the Functional Directorate responsible for the report. For example: Report No. NADC-78015-20 indicates the fifteenth Center report for the year 1978, and prepared by the Systems Directorate. The numerical codes are as follows:

CODE	OFFICE OR DIRECTORATE
00	Commander, Naval Air Development Center
01	Technical Director, Naval Air Development Center
02	Comptroller
10	Directorate Command Projects
20	Systems Directorate
30	Sensors & Avionics Technology Directorate
40	Communication & Navigation Technology Directorate
50	Software Computer Directorate
60	Aircraft & Crew Systems Technology Directorate
70	Planning Assessment Resources
80	Engineering Support Group

**PRODUCT ENDORSEMENT** - The discussion or instructions concerning commercial products herein do not constitute an endorsement by the Government nor do they convey or imply the license or right to use such products.

APPROVED BY:

  
T. J. GALLAGHER  
CAPT, MSC, USN

DATE:

10-29-82

UNCLASSIFIED

SECURITY CLASSIFICATION OF THIS PAGE (When Data Entered)

REPORT DOCUMENTATION PAGE		READ INSTRUCTIONS BEFORE COMPLETING FORM
1. REPORT NUMBER NADC-81106-60	2. GOVT ACCESSION NO. AD-A124 20-1	3. RECIPIENT'S CATALOG NUMBER
4. TITLE (and Subtitle)  V/STOL FOUNTAIN FORCE COEFFICIENT		5. TYPE OF REPORT & PERIOD COVERED  Final Report
		6. PERFORMING ORG. REPORT NUMBER
7. AUTHOR(s)  L. W. Glaze, D. R. Bristow and D. R. Kotansky		8. CONTRACT OR GRANT NUMBER(s)  N62269-81-C-0717
9. PERFORMING ORGANIZATION NAME AND ADDRESS McDonnell Aircraft Company P.O. Box 516 St. Louis, Mo. 63166		10. PROGRAM ELEMENT, PROJECT, TASK AREA & WORK UNIT NUMBERS AIRTASK A320320D/001A/2R023-02-000
11. CONTROLLING OFFICE NAME AND ADDRESS Naval Air Development Center Aircraft and Crew Systems Technology Dir. (6053) Warminster, Pa 18974		12. REPORT DATE January 1983
		13. NUMBER OF PAGES 53
14. MONITORING AGENCY NAME & ADDRESS (if different from Controlling Office)		15. SECURITY CLASS. (of this report)  Unclassified
		15a. DECLASSIFICATION/DOWNGRADING SCHEDULE
16. DISTRIBUTION STATEMENT (of this Report)  Approved for Public Release; Distribution Unlimited		
17. DISTRIBUTION STATEMENT (of the abstract entered in Block 20, if different from Report)		
18. SUPPLEMENTARY NOTES		
19. KEY WORDS (Continue on reverse side if necessary and identify by block number)  V/STOL Suckdown Fountain Impingement Jet Entrainment		
20. ABSTRACT (Continue on reverse side if necessary and identify by block number) The McDonnell Aircraft Company (MCAIR) V/STOL force and moment methodology was applied to a two-jet, a three-jet and a four-jet V/STOL aircraft in hover in ground effect to determine the fraction ( $\lambda_{FI}$ ) of the impinging fountain momentum flux transferred to the airframe as a fountain impingement force. The use of potential flow panel methods was verified for the calculation of suckdown forces on V/STOL aircraft in hover, provided the jet entrainment effects are accurately modeled. In addition, an empirical two-jet fountain		

DD FORM 1473 EDITION OF 1 NOV 65 IS OBSOLETE

UNCLASSIFIED

SECURITY CLASSIFICATION OF THIS PAGE (When Data Entered)

upwash momentum flux distribution was established for use in predicting the magnitude of the impinging fountain momentum flux. Using the MCAIR methodology, the suckdown force and the total momentum flux incident upon the aircraft were calculated, and the results were compared with experimentally measured induced lift to determine  $\lambda_{FI}$  for each aircraft at several heights above ground. The mass entrainment rates associated with an axisymmetric free jet were quantified in an experimental program based upon a new, indirect technique of entrainment measurement. In this new technique, the induced radial velocity field surrounding the free jet was measured using a hot film anemometer. Inverse potential flow theory was then applied to convert the measured radial velocities to free jet mass entrainment rates. This indirect technique substantiated the validity of results obtained by the more conventional, direct method of integrating successive free jet velocity profiles.

## FOREWORD

This study was conducted for the Naval Air Development Center, Warminster, Pennsylvania by the Aerodynamics Department of the McDonnell Aircraft Company (MCAIR), St. Louis, Missouri. The objectives of this study were to determine the fountain impingement momentum flux transfer coefficients associated with three V/STOL aircraft hovering at several aircraft heights in ground effect. The three V/STOL aircraft considered were: (1) the MCAIR YAV-8B, (2) the MCAIR Model 260 and (3) the Grumman Model 698.

The fountain impingement momentum flux transfer coefficients were calculated indirectly by applying the MCAIR V/STOL force and moment prediction methodology which separates the suckdown effects from the fountain impingement effects. This methodology calculates the suckdown force utilizing a potential flow panel method. The fountain impingement force is calculated using a semi-empirical methodology that calculates free jet and wall jet properties (including jet entrainment velocities), predicts the ground wall jet stagnation line location between impinging jet pairs and calculates 2-jet fountain upwash inclination and upwash momentum flux magnitudes. The calculated suckdown and fountain impingement forces were then compared with the total induced lift determined from wind tunnel tests to "back out" the fountain impingement momentum flux transfer coefficient for each of the three aircraft.

The principal investigator of this study was Mr. Lloyd W. Glaze of the McDonnell Aircraft Company Aerodynamics Department. The Naval Air Development Center contract monitor was Mr. Marvin M. Walters.

The authors gratefully acknowledge the NASA Ames Research Center for their cooperation in the conduct of this study and the Grumman Aircraft Corporation for providing configuration information and test results for the Model 698 V/STOL aircraft.

Distribution For MCAIR <input checked="" type="checkbox"/> TAS <input type="checkbox"/> Unannounced <input type="checkbox"/> Identification <input type="checkbox"/>	
Distribution/ Availability Codes Avail and/or Special	
Disb A	

## TABLE OF CONTENTS

<u>Section</u>		<u>Page</u>
I	INTRODUCTION . . . . .	1
II	APPROACH . . . . .	5
	1. SUCKDOWN FORCE CALCULATIONS . . . . .	5
	a. Verification of Suckdown Methodology . . . . .	5
	b. Effect of Lift Jet Paneling . . . . .	10
	c. Corrected Free Jet Entrainment Velocities . . . . .	11
	d. Evaluation of Wall Jet Entrainment Velocities . . . . .	11
	2. FOUNTAIN FORCE CALCULATIONS . . . . .	13
	a. Inner Region Fountain Impingement Momentum Flux . . . . .	16
	b. Outer Region Fountain Impingement Momentum Flux . . . . .	19
III	CALCULATION OF $\lambda_{fi}$ . . . . .	23
	1. YAV-8B . . . . .	23
	2. MCAIR MODEL 260 . . . . .	27
	3. GRUMMAN MODEL 698 . . . . .	27
IV	SUMMARY RESULTS . . . . .	33
V	CONCLUSIONS . . . . .	36
	REFERENCES . . . . .	37
	APPENDIX A . . . . .	39



## LIST OF ILLUSTRATIONS

<u>Figure</u>		<u>Page</u>
1	Flowfield About a VTOL Aircraft Hovering in Ground Effect . . . . .	1
2	Fountain Momentum Flux Recovery . . . . .	3
3	Two-Jet Fountain Inclination - Vertical Impingement . . . . .	3
4	V/STOL Aircraft Selected for Analysis . . . . .	4
5	MCAIR V/STOL Hover Methodology . . . . .	6
6	Paneled Representation of YAV-8B in Hover in Ground Effect . . . . .	7
7	Entrained Mass Flow Distribution for Circular Jets . . . . .	7
8	Pressure Distribution Due to an Axisymmetric Jet Issuing from a Wall . . . . .	8
9	Normal Force Due to an Axisymmetric Jet Issuing from a Flat Plate . . . . .	9
10	Hover Lift Loss Correlation . . . . .	9
11	YAV-8B in Hover Out of Ground Effect . . . . .	10
12	Wall Jet Entrainment Velocities from Original AGSF Program . . . . .	12
13	Wall Jet Entrainment Velocities from Modified AGSF Program . . . . .	12
14	Paneled Representation of Axisymmetric Jet Issuing from a Circular Plate in Ground Effect . . . . .	14
15	Wall Jet Entrainment Velocity Correction Factor . . . . .	14
16	Wall Jet Entrainment Velocity Correction Factor Required to Match Empirical Lift Loss . . . . .	15
17	Summary of Procedure for Calculation of Suckdown Force in Ground Effect . . . . .	15
18	Fountain Impingement Force Calculation Model . . . . .	16
19	Inner Region Fountain Momentum Flux . . . . .	17
20	Fountain Impingement Forces . . . . .	18

## LIST OF ILLUSTRATIONS (Continued)

<u>Figure</u>		<u>Page</u>
21	2-Jet Fountain Spreading Characteristics . . . . .	20
22	2-Jet Fountain Dynamic Pressure Profiles . . . . .	21
23	Empirical 2-Jet Fountain Dynamic Pressure Profile . . . . .	21
24	2-Jet Fountain Upwash Momentum Flux Distribution .	22
25	Paneled Representation of YAV-8B . . . . .	25
26	YAV-8B Induced Lift in Ground Effect . . . . .	25
27	Fountain Impingement Momentum Flux Transfer Coefficient-YAV-8B . . . . .	26
28	Paneled Representation of MCAIR Model 260 . . . . .	28
29	Model 260 Induced Lift in Ground Effect . . . . .	29
30	Fountain Impingement Momentum Flux Transfer Coefficient-Model 260 . . . . .	29
31	Paneled Representation of Grumman Model 698 . . . . .	30
32	Grumman Model 698 Induced Lift in Ground Effect . .	31
33	Fountain Impingement Momentum Flux Transfer Coefficient-Model 698 . . . . .	32
34	Fountain Impingement Momentum Flux Transfer Coefficient Summary . . . . .	34
35	Potential Applications of the Indirect Method of Determining Free Jet Mass Entrainment . . . . .	36
A1	Entrained Mass Flow Distribution for Circular Jets . . . . .	39
A2	Representation of an Axisymmetric Subsonic Jet . .	40
A3	Baseline Nozzle Configuration . . . . .	43
A4	Turbulence Generators . . . . .	44
A5	TSI Model 1330XX Temperature Compensated Hot Film Anemometer Probe . . . . .	45
A6	Nozzle Exit Plane Velocity Profiles (Nozzle A) . .	47

## LIST OF ILLUSTRATIONS (Continued)

<u>Figure</u>		<u>Page</u>
A7	Nozzle Exit Plane Velocity Profiles (Nozzle B) . .	47
A8	Turbulence Intensity and Velocity Profiles (Nozzle B) . . . . .	48
A9	Induced Velocity Measurement Test Hardware (Nozzle A) . . . . .	50
A10	Probe Azimuthal Locations . . . . .	51
A11	Effect of Nozzle Pressure Ratio on Free-Jet Entrainment . . . . .	52
A12	Effect of Turbulence Intensity on $m_1$ . . . . .	52
A13	Comparison of Indirect and Direct Methods for Determining Free-Jet Entrainment . . . . .	53
 <u>Table</u>		 <u>Page</u>
1	Calculated Force Quantities . . . . .	24
A1	Test Program . . . . .	46

LIST OF SYMBOLS, ABBREVIATIONS AND ACRONYMS

$A_{ff}$	- fountain "footprint" area
$A_{fc}$	- fountain cross-sectional area
$D$	- nozzle exit diameter
$D_e$	- equivalent single nozzle diameter (see equation (6))
$\bar{D}$	- angular mean diameter of jet blocking surface
$\bar{D} = \frac{1}{\pi} \int r \, d\phi$	
$F_{fI}$	- fountain impingement force
$F_s$	- suckdown force
$h$	- height above ground measured to the point on the fuselage undersurface directly beneath the aircraft c.g.
$h'$	- height above ground measured to the nozzle exit
$IGE$	- in ground effect
$K_{went}$	- wall jet entrainment velocity correction factor
$\Delta L$	- total induced lift
$\dot{m}$	- mass flux
$\dot{m}_1$	- entrainment rate $(\frac{dm}{dz})$ in potential core region
$\dot{m}_2$	- entrainment rate $(\frac{dm}{dz})$ outside of potential core region
$\dot{M}$	- momentum flux
$NPR$	- nozzle pressure ratio
$OGE$	- out of ground effect
$r$	- radius
$R_I$	- radius of impingement region
$S$	- nozzle exit centerline spacing
$T$	- total thrust
$U$	- wall jet velocity
$\bar{U}$	- free jet axial mean velocity

## LIST OF SYMBOLS, ABBREVIATIONS AND ACRONYMS (Continued)

$U_{CL}$	-	free jet centerline axial velocity
$u'$	-	RMS value of fluctuating free jet axial velocity
$V$	-	velocity
$V_r$	-	radial velocity
$V'$	-	corrected velocity
$x, y, z$	-	cartesian aircraft coordinates (See Figure 4)
$z_c$	-	free jet potential core length
$z'$	-	nozzle centerline axial coordinate
$\zeta, \eta$	-	2-jet fountain upwash cartesian coordinat. (See Figure 21)
$\lambda_M$	-	fountain formation momentum flux recovery    efficient
$\lambda_{fI}$	-	fountain impingement momentum flux transf .    efficient
$\rho$	-	density
$\phi$	-	ground plane azimuthal angle measured about impingement point
$\omega$	-	2-jet fountain upwash inclination

Subscripts

calc	-	calculated
ent	-	entrained
exp	-	experimental
f	-	fountain
fent	-	fountain entrainment
I	-	impingement
in	-	inner region
jc	-	jet centerline
je	-	jet exit
max	-	maximum

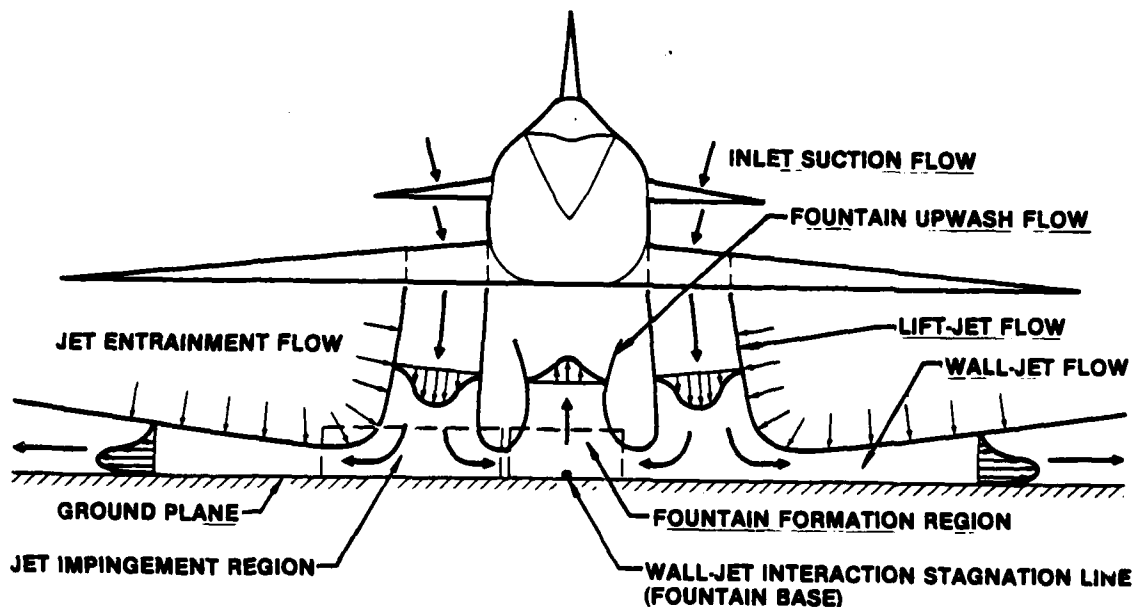
LIST OF SYMBOLS, ABBREVIATIONS AND ACRONYMS (Concluded)

N,n	-	normal
out	-	outer region
R	-	radial
V/2	-	point where velocity equals one half of the maximum value
went	-	wall jet entrainment
wj	-	wall jet

## SECTION I

## INTRODUCTION

The successful design and development of V/STOL aircraft equipped with powered jet lift systems requires a knowledge of the complex flow field interactions produced by these multiple jet lift systems in the hover mode both in and out of ground effect (Figure 1). The accurate prediction of the induced forces and moments on the aircraft is necessary in order to assure that the propulsion system, control system, and other subsystems may be properly designed. A key element in the analytical modeling of these flow fields in ground effect is the formation and development of fountain upwash flows. The prediction of the trajectory of the fountain upwash is also of importance for the computation of moments and in order that lift jet system exhaust reingestion may be minimized. A considerable amount of progress has been made by the McDonnell Aircraft Company (MCAIR) toward the prediction of the complete forces and moments induced on a V/STOL aircraft operating in the hover mode through dedicated experimental and analytical studies conducted through various Contracted Research and Development (CRAD), as well as MCAIR Independent Research and Development (IRAD) programs.



GP23-0302-33

Figure 1. Flowfield About a VTOL Aircraft Hovering in Ground Effect

These research efforts resulted in the development and refinement of the MCAIR multi-jet V/STOL aircraft force and moment methodology, developed for the Naval Air Development Center (NAVAIRDEVCE) in Reference (1). Originally developed for round

jets, this methodology was subsequently expanded under contracts to the NASA Ames Research Center to include propulsive lift systems employing rectangular nozzles with exit area aspect ratios between one and eight (References 2 and 3). The approach in this methodology is to separate the jet entrainment induced suckdown forces from the fountain impingement forces. The former are determined from the jet entrainment induced potential flow field utilizing a multiple boundary condition panel methodology, while the latter are determined from empirical jet impingement data and momentum conservation principles with the inclusion of empirically determined fountain upwash formation momentum loss and fountain upwash airframe impingement coefficients. This empirical/theoretical analysis is embodied in the MCAIR Aircraft/Ground/Stagnation Line/Fountain (AGSF) methodology (Reference 4).

A recent experimental investigation conducted by MCAIR for the Office of Naval Research (ONR) (Reference 5) yielded two fundamentally significant modeling elements: (1) experimentally determined fountain formation momentum flux recovery coefficients, and (2) a verified analytical model for the fountain upwash flow trajectory. The fountain momentum flux recovery coefficient,  $\lambda_M$ , is the ratio of local momentum flux in the fountain upwash to the total local momentum flux entering the fountain base from the ground wall jets.  $\lambda_M$  is shown as a function of jet pair exit momentum flux ratio (or thrust bias),  $M_{j\text{LOW}}/M_{j\text{HIGH}}$  in Figure 2. These data indicate that approximately 45% of the momentum flux entering the fountain formation region between two equal, vertically impinging jets is not available in the fountain upwash flow, ( $\lambda_M \approx 0.55$ ). Figure 3 presents the variation of the 2-jet fountain inclination ( $\omega$ ) as a function of the jet pair exit momentum flux ratio for various values of  $\lambda_M$  along with experimental verification. The dashed line in Figure 3 represents the fountain inclination based on the curve fit value of  $\lambda_M$  shown in Figure 2.

The establishment of the above ground flow field modeling elements, together with recent improvements made to potential flow panel methods for the determination of jet entrainment induced suckdown, leaves only one empirical element remaining to complete the prediction methodology for a wide range of V/STOL aircraft configurations. This remaining element is the quantification of the amount of momentum flux transferred to the airframe under-surface from the upwash momentum flux in the fountain. This quantity,  $\lambda_{fI}$ , is termed the fountain upwash momentum flux transfer coefficient.

The fountain impingement momentum flux transfer coefficient was determined for the YAV-8B in hover at one height in ground effect as part of a recent MCAIR Independent Research and Development (IRAD) Project. The present contract study includes the calculation of  $\lambda_{fI}$  for the YAV-8B aircraft at three additional heights in ground effect. Furthermore,  $\lambda_{fI}$  was calculated for the



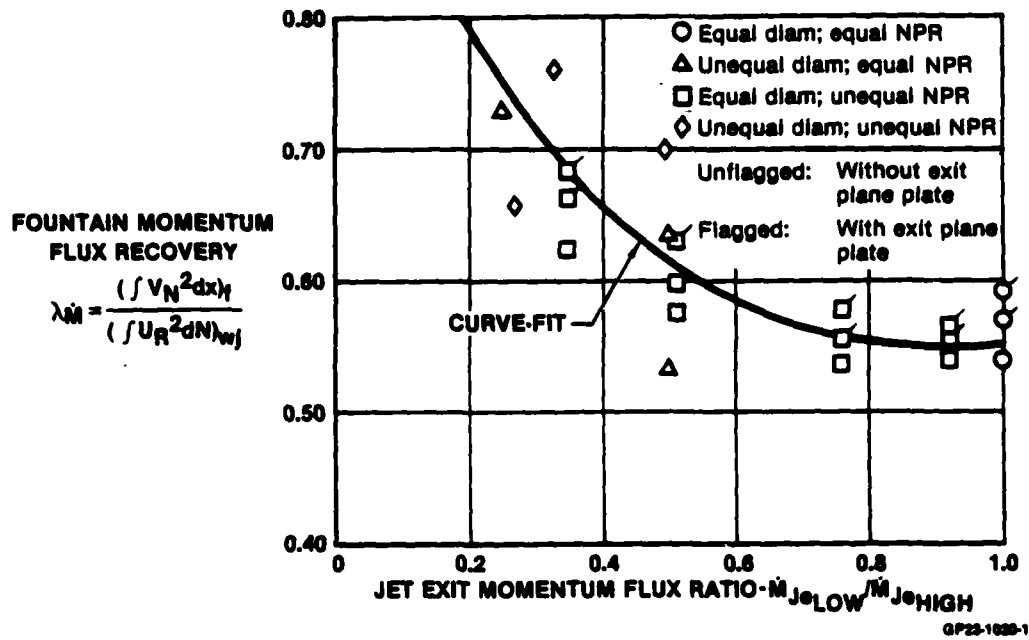


Figure 2. Fountain Momentum Flux Recovery Based on Conservation of Mass Flux Through the Fountain Formation Region

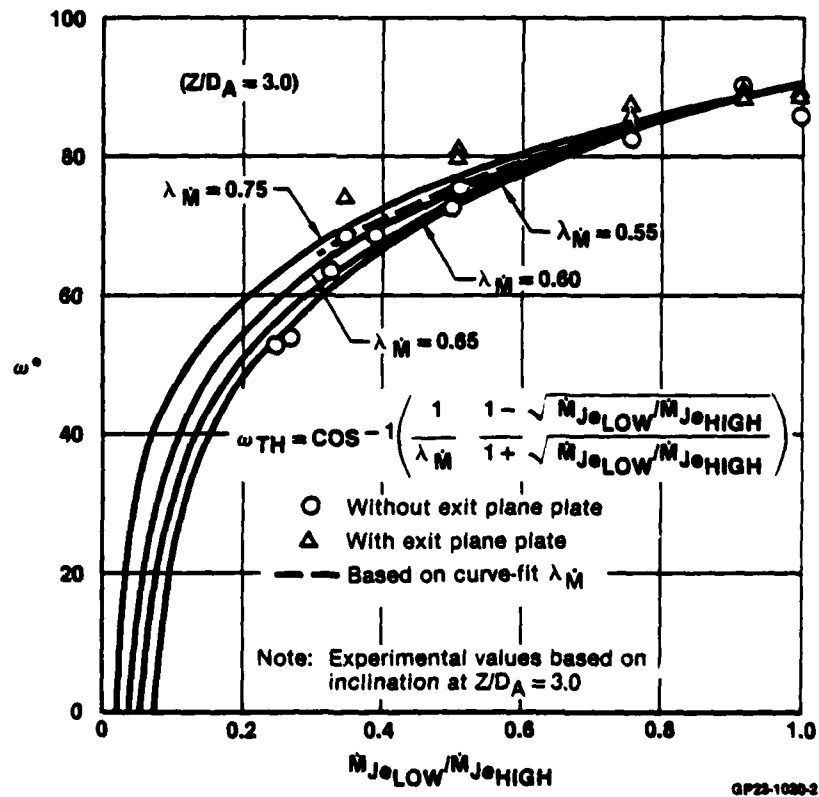


Figure 3. Two-Jet Fountain Inclination - Vertical Impingement

MCAIR Model 260 3-jet V/STOL aircraft at three heights in ground effect and for the Grumman Model 698 2-jet V/STOL aircraft at five heights in ground effect. The three aircraft configurations are illustrated in Figure 4.

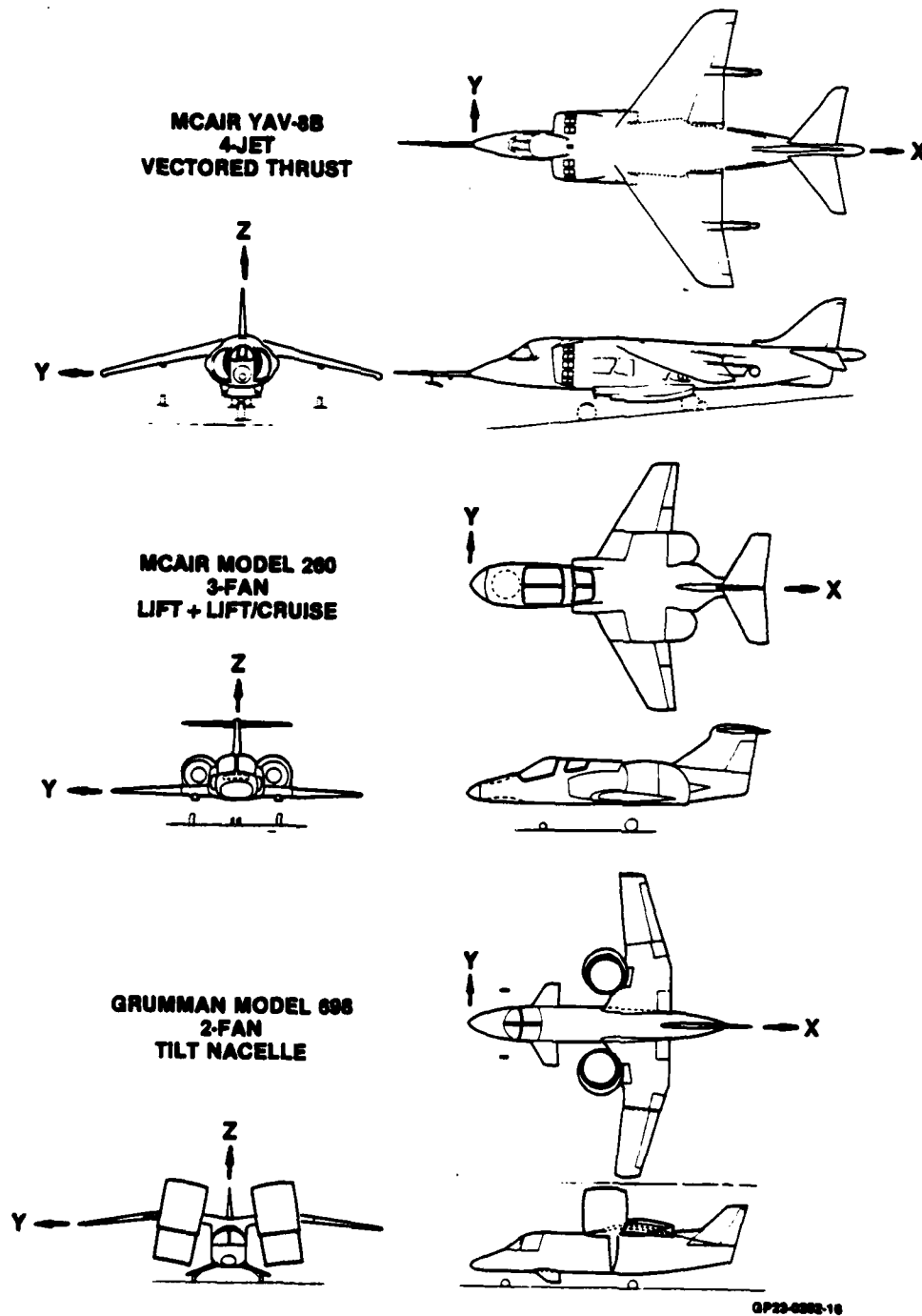


Figure 4. V/STOL Aircraft Selected for Analysis

## SECTION II

## APPROACH

The MCAIR V/STOL hover methodology is illustrated for a two-jet configuration in Figure 5. The total thrust non-dimensionalized jet induced lift ( $\Delta L/T$ ) is defined as the sum of the non-dimensionalized jet entrainment induced suckdown force ( $F_s/T$ ) and the non-dimensionalized fountain impingement force ( $F_{fI}/T$ ). The fountain impingement force is in turn defined as the product of the fountain impingement momentum flux transfer coefficient ( $\lambda_{fI}$ ) and the total fountain upwash momentum flux ( $\dot{M}_{fI}/T$ ) incident upon the aircraft; thus,

$$\frac{\Delta L}{T} = \frac{F_s}{T} + \lambda_{fI} \frac{\dot{M}_{fI}}{T} \quad (1)$$

The approach taken in this study is to calculate the suckdown force,  $F_s/T$ , and the fountain upwash momentum flux,  $\dot{M}_{fI}/T$ , and by applying equation (1), compare their sum to experimentally determined values of the total induced lift,  $\Delta L/T$ , to "back out" the corresponding value of  $\lambda_{fI}$ . This was done for the three aircraft illustrated in Figure 4 for at least three aircraft heights above ground each. The procedures used to calculate  $F_s/T$  and  $\dot{M}_{fI}/T$  are described below.

1. SUCKDOWN FORCE CALCULATIONS - To calculate the suckdown force on a V/STOL aircraft hovering in ground effect, the aircraft, lift jet and wall jet surfaces are paneled for use with a surface singularity panel method. Figure 6 presents the paneled representation of the YAV-8B in hover in ground effect. The panel methodology selected for use in this study is a modified version of the PAN AIR surface singularity methodology of Reference 6. The modification permits the specification of non-zero normal velocity boundary conditions on jet surface panels to represent jet entrainment flow. Zero flow normal to the panel surface is prescribed as the boundary condition on aircraft surfaces. The suckdown methodology was verified and the entrainment models utilized by the AGSF program were investigated prior to applying the methodology to the complete aircraft configurations.

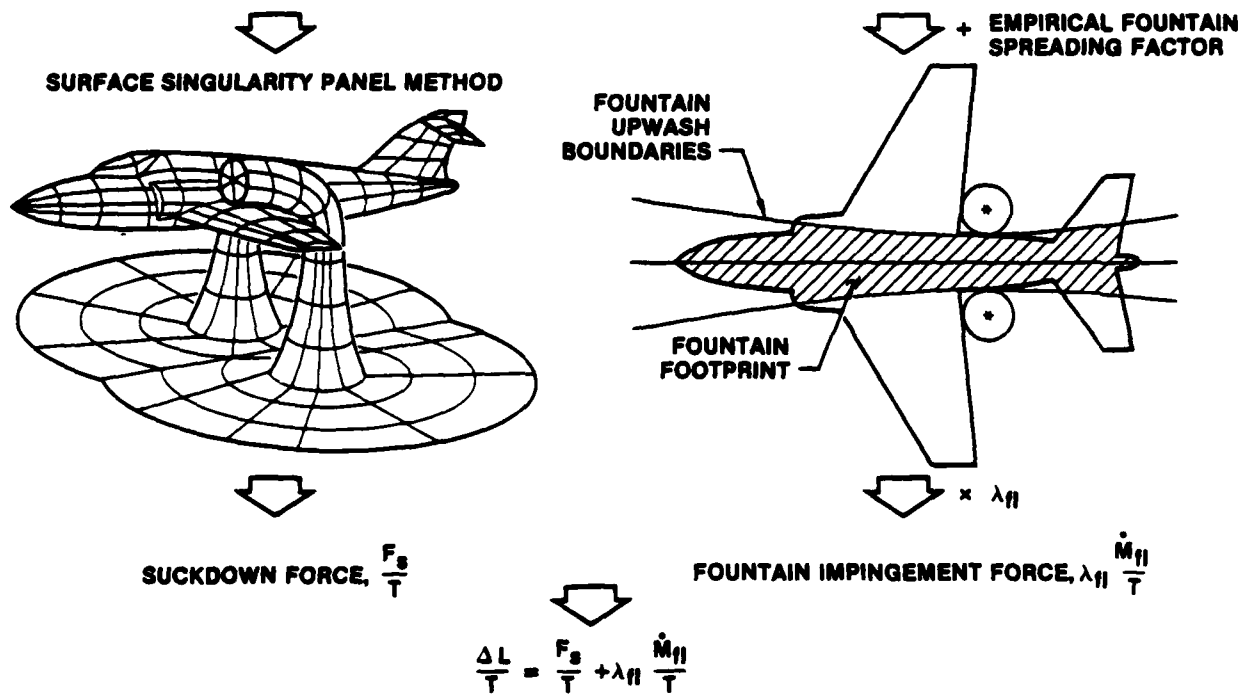
a. Verification of Suckdown Methodology - In order to verify the validity of this approach when applied to aircraft in hover ( $V_\infty=0$ ), a simple test case consisting of an axisymmetric jet issuing from an infinite flat plate into static air was modeled. The pressure distribution on the surface of the plate was calculated using two different, empirically determined, axisymmetric jet mass entrainment models. Figure 7 presents the entrained mass flow distributions determined for a circular jet in five separate

previous investigations. The wide disparity in the curves illustrates the uncertainty in the measurement of such data. Figure 8 compares the pressure distributions calculated by a panel method using the entrainment curves of Wygnanski and of Kleis and Foss with experimental plate surface pressure data determined by Wygnanski. The curves illustrate the effect of varying the free jet mass entrainment rate on the flat plate pressure distribution.

**AIRCRAFT/GROUND/STAGNATION LINE/FOUNTAIN  
(AGSF) PROGRAM CALCULATES:**

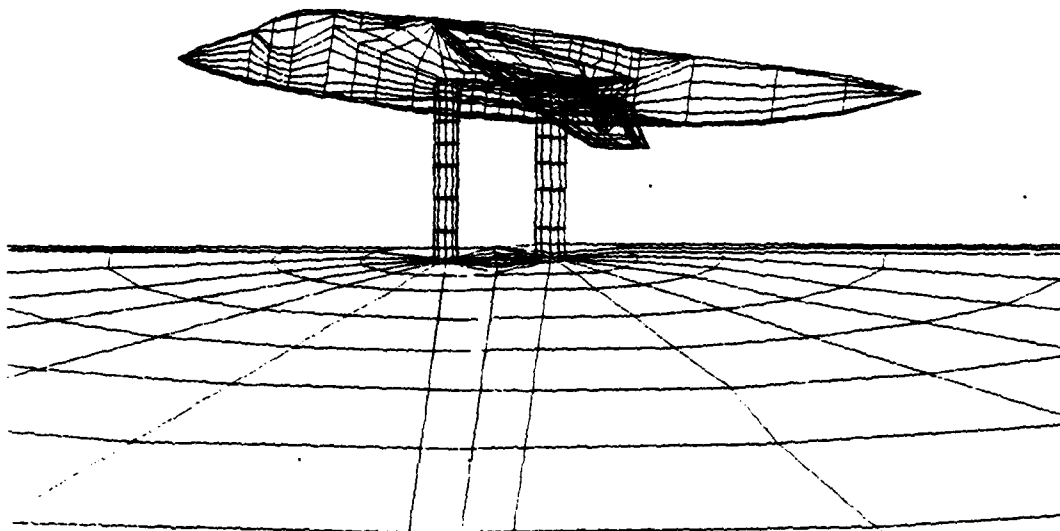
- FREE JET ENTRAINMENT VELOCITIES
- WALL JET ENTRAINMENT VELOCITIES

- JET IMPINGEMENT POINTS
- STAGNATION LINE LOCATIONS
- FOUNTAIN UPWASH DIRECTION
- FOUNTAIN UPWASH MOMENTUM FLUX



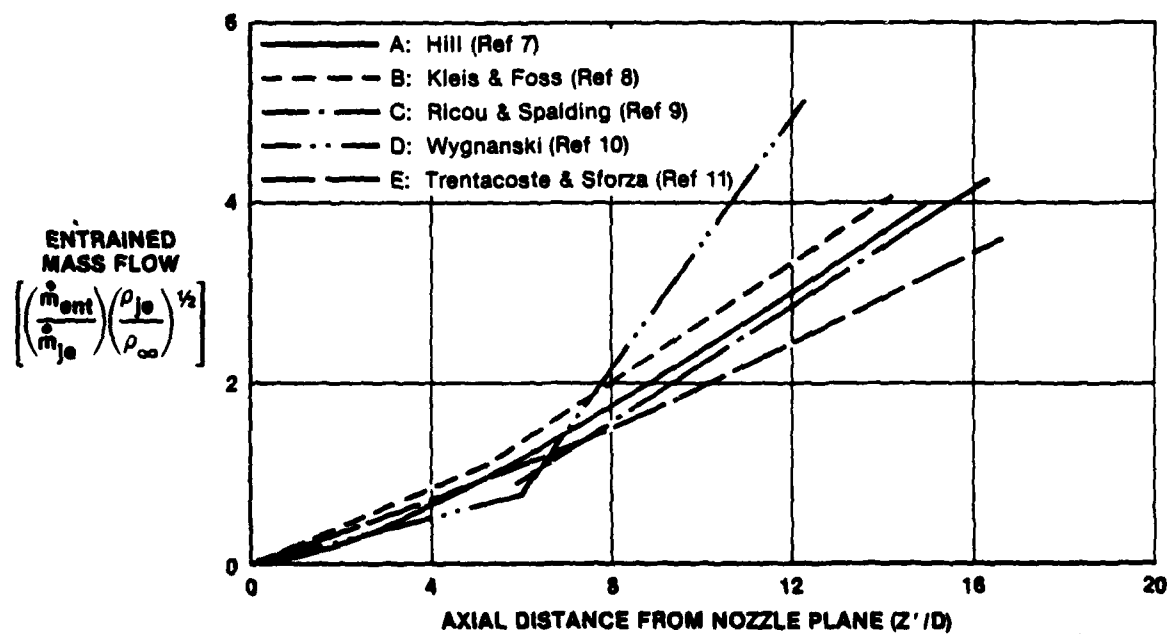
GP23-0202-17

Figure 5. MCAIR V/STOL Hover Methodology



GP23-0202-19

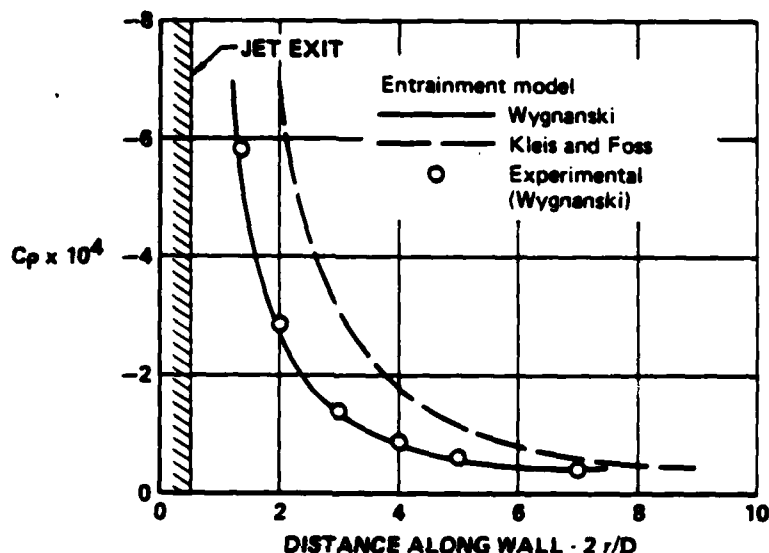
Figure 6. Paneled Representation of YAV-8B in Hover in Ground Effect  
 $h/D_0 = 2.76$



GP23-0202-31

Figure 7. Entrained Mass Flow Distribution for Circular Jets

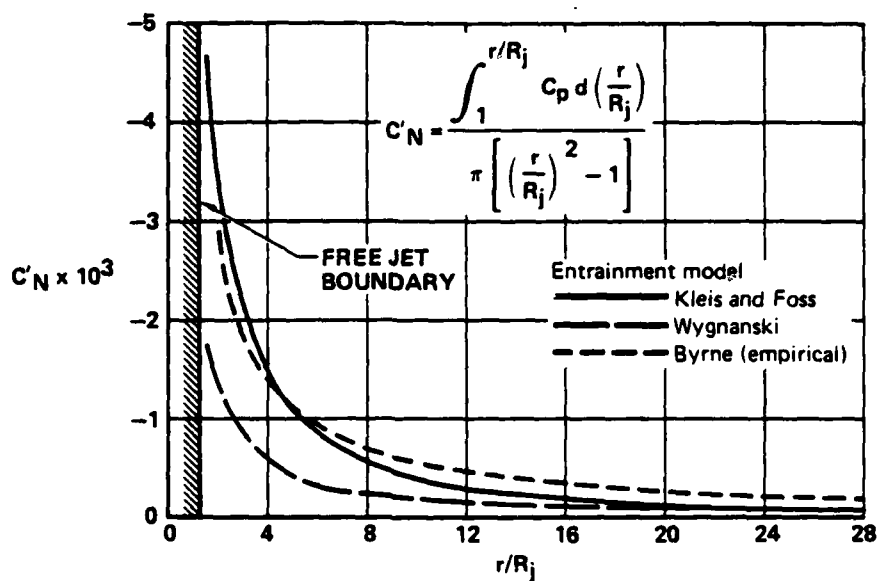
In both of the calculated cases shown in Figure 8, the mass entrainment rate was considered to be constant within the potential core region ( $Z/D < 6$ ) and constant outside the potential core region ( $Z/D > 6$ ) with the higher entrainment rate occurring in the fully developed region. The accuracy with which the panel method (in conjunction with Wygnanski's entrainment model) reproduces Wygnanski's empirical curve demonstrates the validity of the panel method for use in hover.



GP13-60000-4

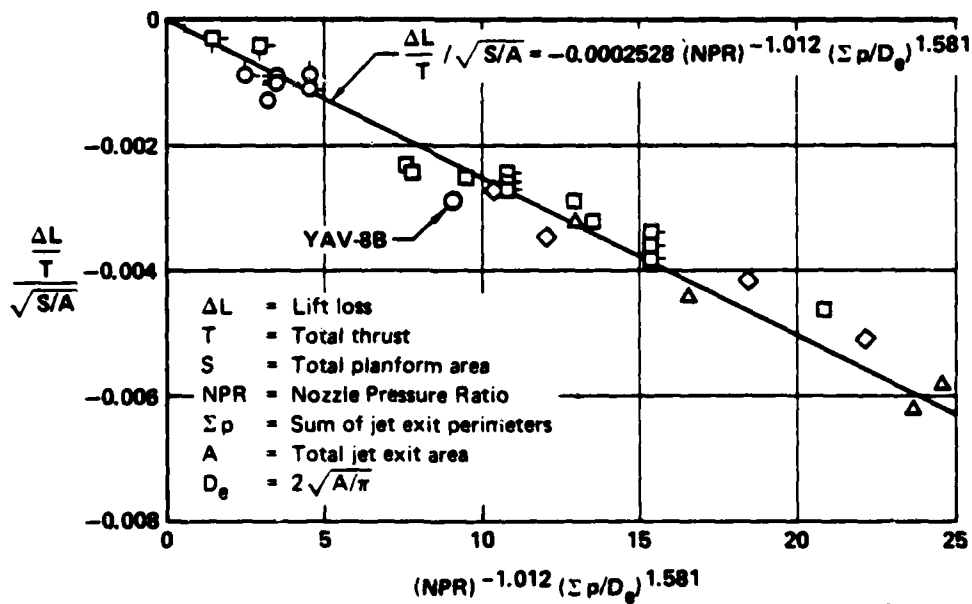
Figure 8. Pressure Distribution Due to an Axisymmetric Jet Issuing from a Wall

The calculated pressure distributions were integrated as a function of radial distance along the plate to yield a normal force coefficient ( $C_N$ ). The variation of integrated normal force with radial distance is illustrated in Figure 9 for the two entrainment models. Also shown in Figure 9 is the normal force on the plate induced by a single circular jet (operating at the same conditions as the test case) determined from the empirical relation derived by Byrne (Reference 12). This relationship (shown in Figure 10) represents a correlation of induced lift data obtained experimentally for several V/STOL aircraft models in hover out of ground effect. The normal force curves of Figure 9 indicate that both entrainment models tend to underpredict the actual jet induced force. It was concluded from this study that the potential flow representation of jet induced suckdown is valid, but the existing empirical entrainment distributions are too weak and must be corrected to accurately model jet induced forces. As a result of this finding, an experimental test program was conducted using a new technique to indirectly measure axisymmetric free jet entrainment using a hot film anemometer. The experimental test program and test results are discussed in Appendix A. A procedure for correcting existing entrainment distributions for calculating suckdown forces in hover in ground effect (IGE) is presented in Section II.1.C.



GP13-0002-4

Figure 9. Normal Force Due to an Axisymmetric Jet Issuing from a Flat Plate



GP23-0002-4

Figure 10. Hover Lift Loss Correlation

b. Effect of Lift Jet Paneling - The effect of the lift jet paneling geometry was investigated using the paneled model of the YAV-8B aircraft in hover out of ground effect (OGE). Figure 11 illustrates the paneled aircraft with two possible paneled jet models. In one case, the paneling represents the spreading jet geometry calculated by the AGSF program. In the other case, an equivalent cylindrical jet paneling was applied. The entrainment data of Kleis and Foss was utilized for both cases. It was verified that both paneled jet representations generate the same calculated suckdown force on the aircraft,  $\frac{\Delta L}{T} = -.006$ . This confirms that the simple cylindrical jet paneling is entirely adequate, provided that the jet normal velocity (entrainment) distribution is adjusted to account for the smaller jet perimeter. However, the experimentally measured suckdown force on the YAV-8B in hover OGE is  $-.020$ , substantially larger than predicted. This result reemphasizes the result determined using the infinite flat plate model that existing empirical free jet entrainment rates underestimate actual entrainment and require adjustment.

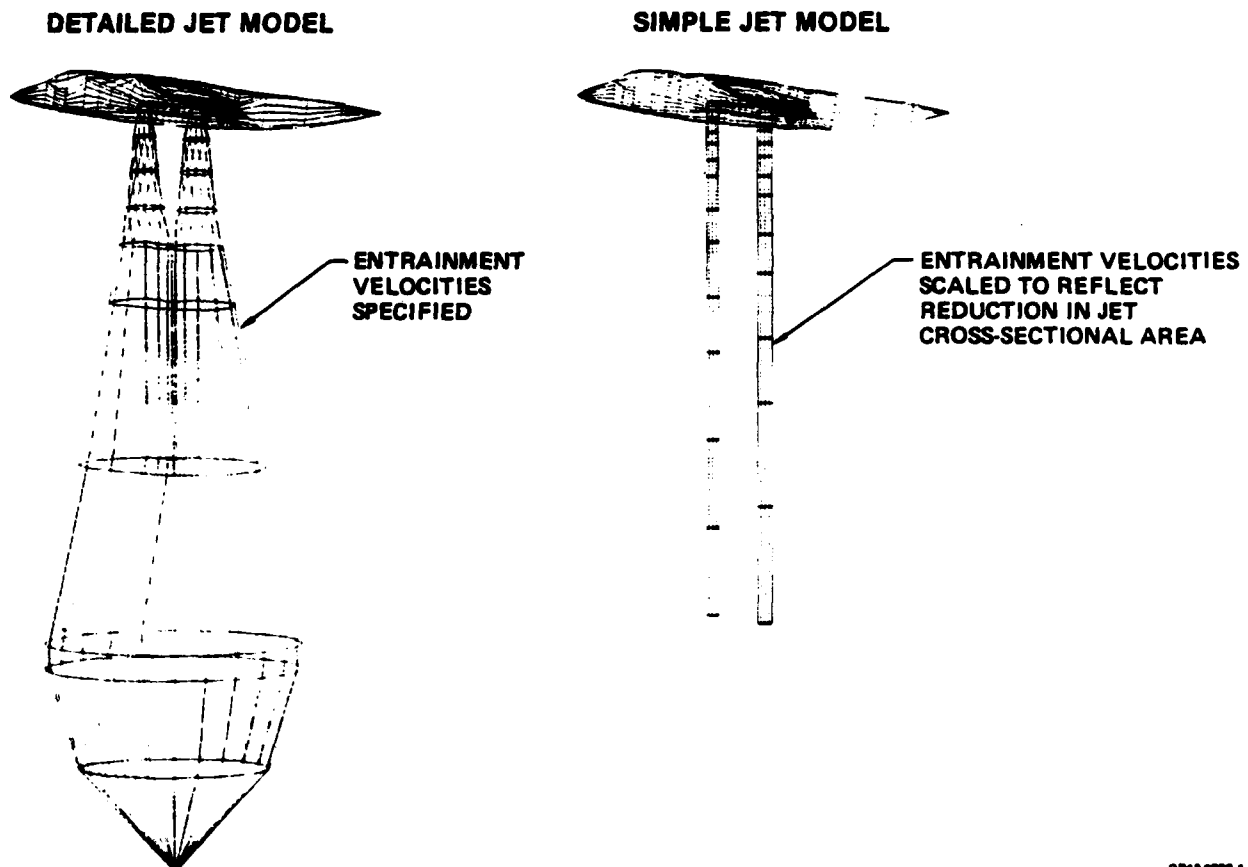


Figure 11. YAV-8B in Hover Out of Ground Effect  
Alternate Jet Models

GP13-0882-4



c. Corrected Free Jet Entrainment Velocities - Due to the uncertainty in empirical distributions of free jet entrainment rates (Figure 7), the free jet entrainment velocities utilized to calculate suckdown forces in hover IGE are based on corrected values of the free jet entrainment velocities ( $V_{fent}$ ) utilized for hover OGE. In this procedure, the suckdown force out of ground effect ( $\frac{F_s}{T}$ ) is calculated using the entrainment data of Kleis and Foss. The result is then compared with experimental data (or, if such data is not readily available, with the general curve developed by Byrne [Reference 12], Figure 10) to yield the corrected free jet entrainment velocity,  $V'_{fent}$ , as follows:

$$V'_{fent} = \sqrt{\frac{(\Delta L/T)_{exp}}{(F_s/T)_{calc}}} V_{fent} \quad (\text{out of ground effect}) \quad (2)$$

d. Evaluation of Wall Jet Entrainment Velocities - As originally calculated by the AGSF program, the wall jet entrainment velocities ( $V_{went}$ ) varied directly with the radius of the jet impingement region ( $R_I$ ) and the free jet centerline velocity at impingement ( $V_{jcl}$ ) and inversely with radius ( $r$ ); i.e.,

$$V_{went} \propto \left( \frac{R_I V_{jcl}}{r} \right) \quad (3)$$

Although this relation provides the correct variation of  $V_{went}$  with radial distance (Figure 12), the variation of  $V_{went}$  with nozzle height ( $h/D$ ) is the opposite of that which would be expected. This unreasonable variation was found to result from the fact that  $R_I$  increases more rapidly than  $V_{jcl}$  decreases with respect to increasing  $h/D$ . The expression for  $V_{jcl}$  is based upon empirical data and is generally assumed to be accurate. Consequently,  $V_{went}$  was redefined, in a manner consistent with the formulation in Reference 1, as:

$$V_{went} \propto \left( \frac{2.4D V_{jcl}}{r} \right) \quad (4)$$

(where 2.4D represents the radius of the impingement region at  $h/D = 4$ ). Figure 13 illustrates that the revised wall jet entrainment velocities exhibit the correct variation of  $V_{went}$  with  $h/D$ . It should also be noted that  $V_{went}$  is invariant with  $h/D$  for  $h/D \leq 6$ . The reason for this is that the impinging jet centerline flow is still within the potential core, where  $V_{jcl}$  is constant.

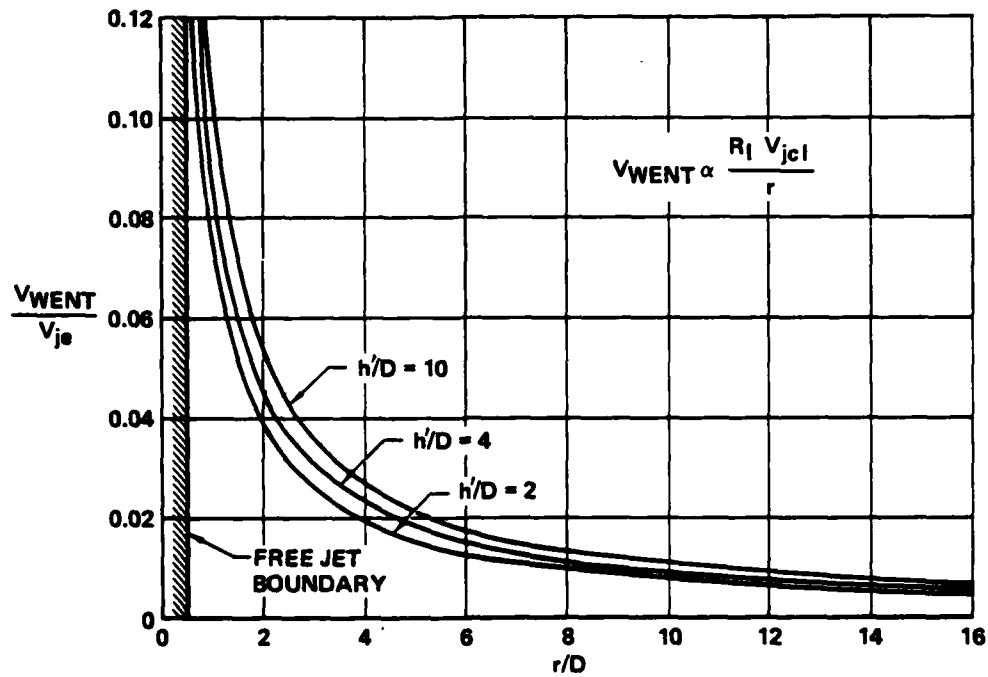


Figure 12. Wall Jet Entrainment Velocities  
From Original AGSF Methodology  
(NPR = 2.0)

GP13-0002-9

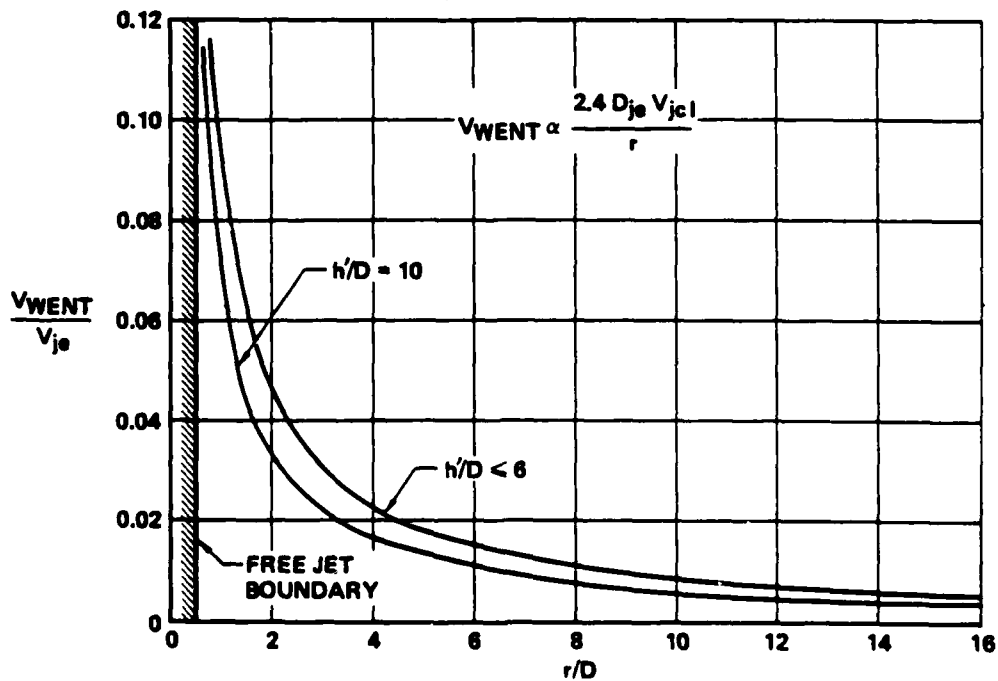


Figure 13. Wall Jet Entrainment Velocities  
from Modified AGSF Methodology  
(NPR = 2.0)

GP13-0002-10

In order to verify the accuracy of the magnitude of  $V_{went}$ , a simple test case was devised for use with the panel methodology. The test case (shown schematically in Figure 14) consisted of a circular disk (with diameter  $\bar{D}$ ) emitting an axisymmetric jet (with diameter  $D$ ) in ground effect. The free jet entrainment velocities used were the corrected free jet entrainment velocities,  $V'_{fent}$ , defined by equation (2). The suckdown force on the disk was then calculated using the wall jet entrainment velocities,  $V_{went}$ , of Figure 13 multiplied by various constant scaling factors,  $K_{went}$ . The variation of the calculated induced lift  $F_s/T$ , with  $K_{went}$  is shown in Figure 15 for a disk-to-jet diameter ratio ( $\bar{D}/D$ ) of 8 and for disk heights of two and four jet diameters above the ground plane. The dashed lines in the figure represent the induced lift determined using the following empirical relation (from Reference 12):

$$\frac{F_s}{T} = - .015 \left[ \frac{h/D_e}{(\bar{D}/D_e - 1)} \right] \exp \{ - [2.2 - .24 (NPR - 1)] \} \quad (5)$$

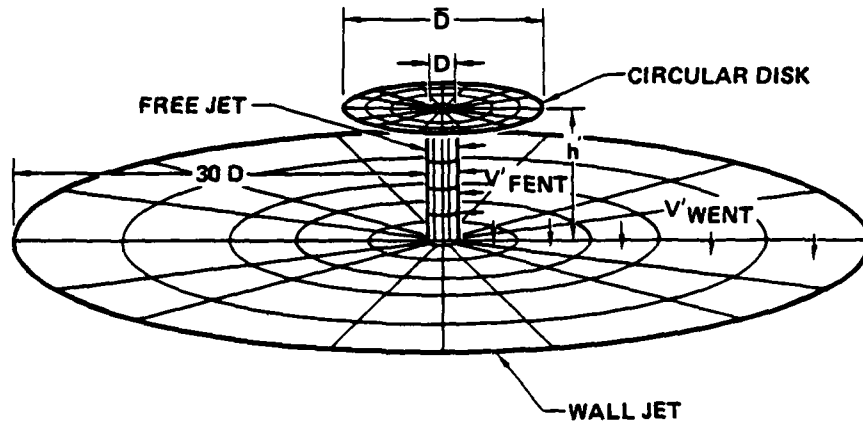
The diameter,  $D_e$ , represents the equivalent single nozzle exit diameter and is defined as:

$$D_e = 2 \sqrt{\frac{\sum_{i=1}^n A_{jei}}{\pi}} \quad (6)$$

where  $A_{jei}$  is the nozzle exit area of the  $i$  th nozzle and  $n$  is the number of jets. It should be noted that for the single axisymmetric nozzle shown in Figure 14,  $D$  is equivalent to  $D_e$ .

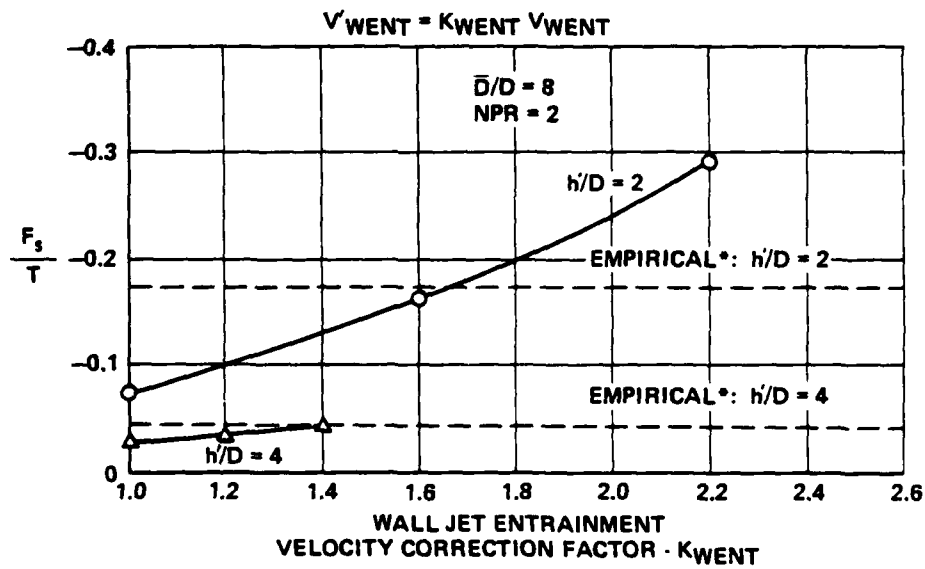
The points in Figure 15 at which the curves cross the dashed lines determine the value of  $K_{went}$  required for adjustment of the uncorrected wall jet entrainment velocities ( $V_{went}$ ) to yield the empirical value of the induced lift. Curves such as those shown in Figure 15 were also obtained for  $\bar{D}/D_e = 6$  and  $\bar{D}/D_e = 12$  at  $h/D_e = 2$  and 4. The value of  $K_{went}$  required to match the empirical lift loss in ground effect is shown in Figure 16 as a function of plate diameter,  $\bar{D}/D_e$ . A value of  $K_{went} = 1.50$  was selected for use in all future cases in this study. Figure 17 presents a summary of the procedure used to calculate the total suckdown force on V/STOL aircraft hovering in ground effect.

**2. FOUNTAIN FORCE CALCULATIONS** - Using the MCAIR V/STOL force prediction methodology, the total multiple jet fountain upwash momentum flux incident upon the aircraft,  $\dot{M}_{fI}$ , is calculated as the sum of an inner region contribution  $\dot{M}_{fIin}$  and an outer region contribution,  $\dot{M}_{fIout}$ . The fountain upwash momentum flux contributions emanating from the inner region and outer region are determined graphically (Figure 18) using the data determined using the AGSF methodology. However, only a fraction of the total impinging fountain momentum flux is converted to a force on the aircraft. This fraction is accounted for in the methodology by employing the fountain impingement momentum flux coefficient,  $f_I$ .



GP13-0902-11

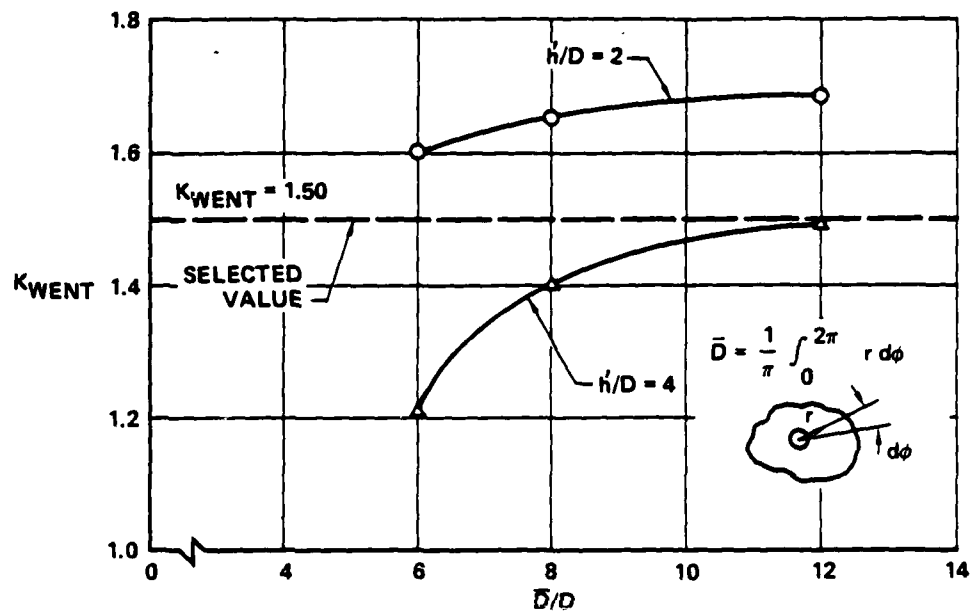
Figure 14. Paneled Representation of Axisymmetric Jet Issuing from a Circular Plate in Ground Effect



$$\frac{F_s}{T} = -0.015 \left( \frac{h/D_e}{(\bar{D}/D_e - 1)} \right) \cdot [2.2 - 0.24 (NPR - 1)]$$

GP13-0902-12

Figure 15. Wall Jet Entrainment Velocity Correction Factor



GP13-0002-2

Figure 16. Wall Jet Entrainment Velocity Correction Factor Required to Match Empirical Lift Loss  
Circular Plate IGE

#### MCAIR SUCKDOWN METHODOLOGY:

1. PANEL AIRCRAFT AND LIFT JETS
2. DETERMINE  $(\Delta L/T)_{CALC}$  OUT OF GROUND EFFECT (OGE) USING UNCORRECTED  $V_{FENT}$  OF KLEIS AND FOSS
3. CORRECT  $V_{FENT}$  TO MATCH EMPIRICAL LIFT LOSS,  $(\Delta L/T)_{EXP}$ , AS:

$$V'_{FENT} = \sqrt{\frac{(\Delta L/T)_{EXP}}{(\Delta L/T)_{CALC}}} V_{FENT}$$

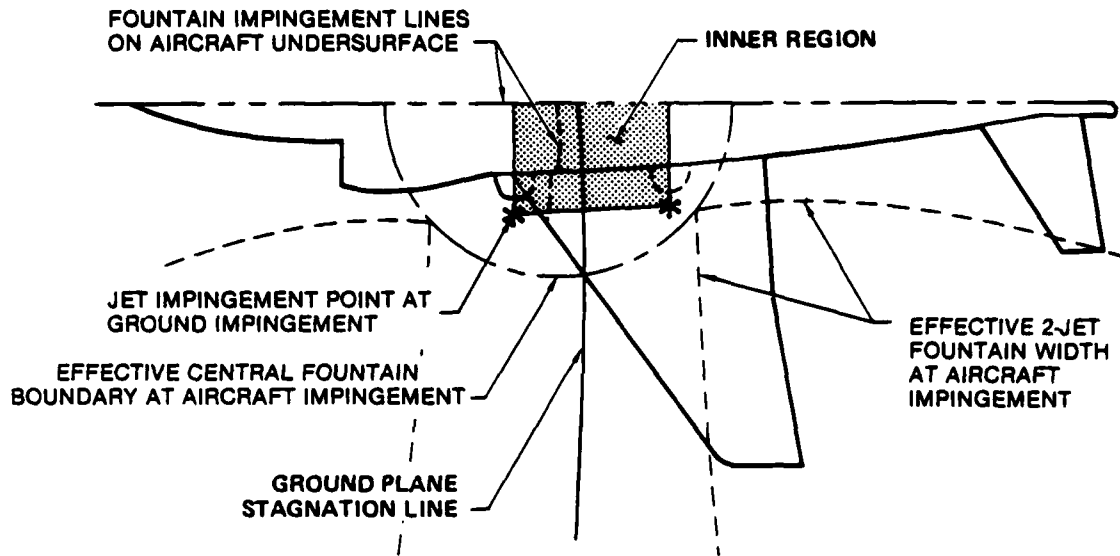
4. PANEL WALL JETS
5. DETERMINE  $V_{WENT}$  USING AGSF PROGRAM AND CORRECT AS:

$$V'_{WENT} = 1.5 V_{WENT}$$

6. CALCULATE TOTAL SUCKDOWN FORCE IGE,  $F_S$ , USING PANEL METHOD WITH  $V'_{FENT}$  AND  $V'_{WENT}$

GP13-0002-14

Figure 17. Summary of Procedure for Calculation of Suckdown Force in Ground Effect



GP13-0802-17

Figure 18. Fountain Impingement Force Calculation Model

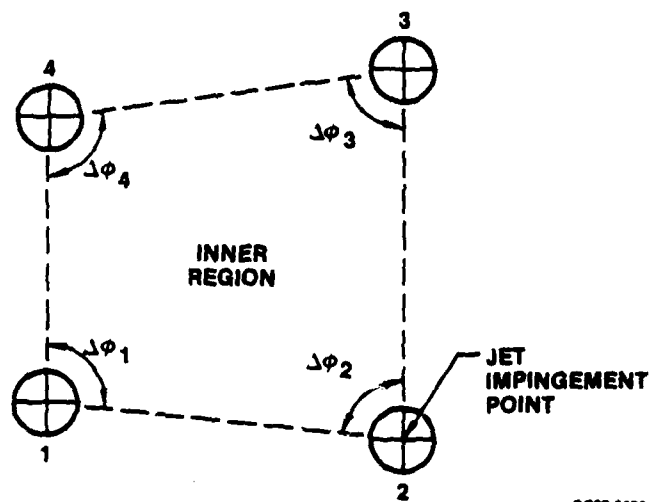
a. Inner Region Fountain Impingement Momentum Flux - To calculate  $\dot{M}_{fin}$ , all of the wall jet momentum flux within the inner region is assumed to be turned upward in a central fountain. Due to the lack of sufficient experimental data to define multiple jet central fountain characteristics, the central fountain is assumed to be circular in cross section and to exhibit the same spreading characteristics as described below for the two-jet fountain. The total momentum flux contained within the central fountain upwash is determined as (see Figure 19):

$$\dot{M}_{fin} = \lambda_M \sum_{i=1}^n \frac{\Delta \phi_i}{2\pi} \dot{M}_{jei} \quad (7)$$

where  $\dot{M}_{je}$  is the jet exit momentum flux,  $\lambda_M$  is the fountain formation momentum flux recovery factor determined for two-jet fountains in Reference 5 and  $n$  is the number of lift jets. (The factor  $\lambda_M$  was found to be equal to approximately .55 for two jets impinging vertically with equal thrust and this value increased as the thrust differential between the two impinging jets increased; see Figure 2.) The inner region fountain impingement momentum flux is then calculated based on the ratio of the cross-sectional area of the central fountain at impingement,  $A_{fc}$ , and the planform area intercepted by the central fountain,  $A_{ff}$  as (see Figure 20):

$$\dot{M}_{fin} = \left( \frac{A_{ff}}{A_{fc}} \right) \dot{M}_{fin} \quad (8)$$

$$\dot{M}_{fIN} = \lambda \dot{M} \sum_{i=1}^n \frac{\Delta\phi_i}{2\pi} \dot{M}_{jei}$$

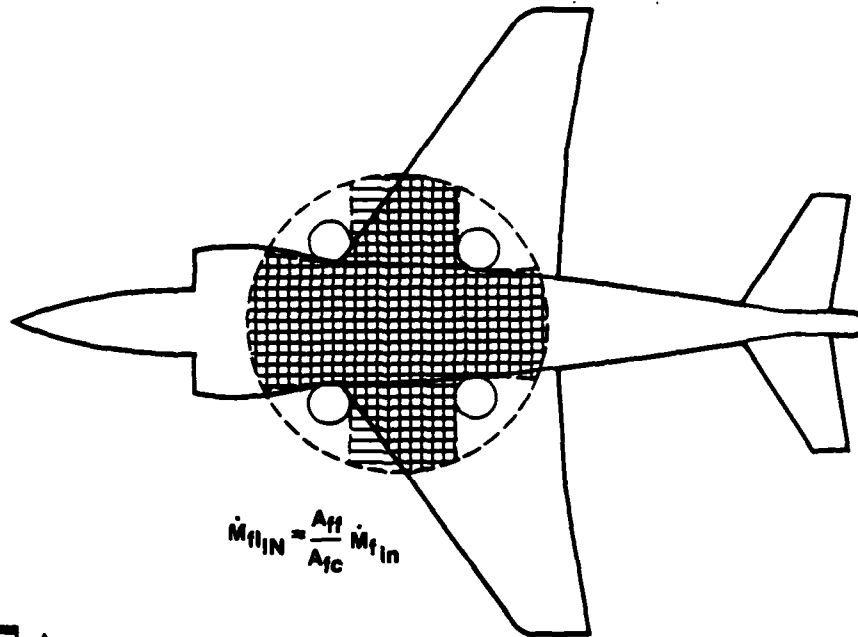


GP23-4202-16

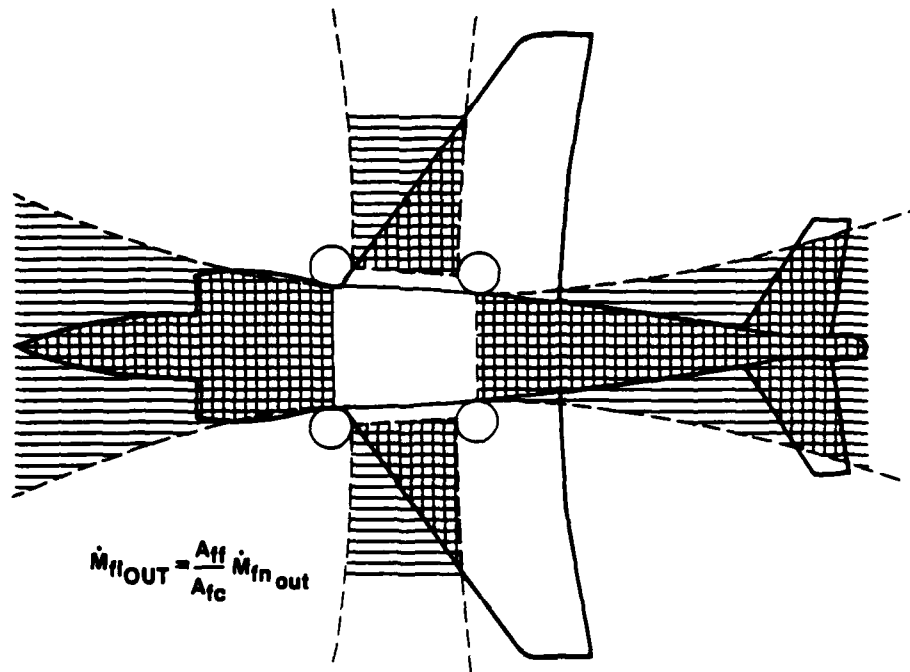
Figure 19. Inner Region Fountain Momentum Flux

NADC-81106-60

INNER REGION



OUTER REGION



GP23-1020-4

Figure 20. Fountain Impingement Forces  
Uniform Momentum Flux Distribution



b. Outer Region Fountain Impingement Momentum Flux - To calculate  $M_{fIout}$ , the fountain upwash momentum vectors are projected upward from the ground plane stagnation line to intersect the aircraft planform yielding the fountain impingement centerline (Figure 18). Application of an empirical two-jet fountain spreading rate yields the effective fountain upwash boundaries and, consequently, the fountain "footprint" or that area of the aircraft planform intercepted by the fountain upwash. The two-jet fountain spreading rate was determined based on the data obtained in Reference 5 (see Figure 21) and is given as:

$$\frac{\eta f}{D} \approx 2 \frac{\eta v/2}{D} \quad (9)$$

where

$$\frac{\eta v/2}{D} = .50 + .35 \frac{z}{D} \quad (10)$$

Previously, the fountain impingement momentum flux in the outer region was also calculated using the simple area ratio between the fountain "footprint" area  $A_{ff}$ , and the fountain cross-sectional area at impingement,  $A_{fc}$ , (Figure 20) with:

$$M_{fIout} = \frac{A_{ff}}{A_{fc}} \times M_{fnout} \quad (11)$$

where  $M_{fnout}$  represents the vertical momentum flux contained within the fountain upwash in the outer region. This definition of  $M_{fIout}$  inherently assumes a uniform distribution of momentum flux across the fountain. The apparent overlap of the cross-hatched areas of the inner region and outer region computational models shown in Figure 20 accounts for the mixing between the two-jet upwash flow and the central fountain flow.

Recently, however, a more accurate, non-uniform fountain momentum flux distribution curve was developed under IRAD based on a correlation of existing 2-jet fountain upwash dynamic pressure profiles obtained in Reference 5 and in an unpublished IRAD experimental program. Figure 22 presents the dynamic pressure profiles obtained for a nozzle exit spacing of  $s/D = 12.8$  and nozzle exit height of  $h/D = 5.0$  and for  $s/D = 7.49$  and  $h/D = 8.0$ . The figure illustrates that the dynamic pressure profiles are similar for variations in fountain height  $\frac{z}{D}$  and, in fact, are essentially similar for variations in  $s/D$  and  $h/D$  as well. Consequently, based upon these correlations, a single, empirical 2-jet fountain dynamic pressure profile (Figure 23) was derived. This empirical fountain dynamic pressure profile was then integrated with respect to the fountain width,  $\eta$ , to yield the 2-jet fountain upwash momentum flux distribution shown in Figure 24. The decrease in slope of the distribution curve shown in Figure 24 with  $\eta$  indicates the decreased impact of the fountain upwash along the fountain outer edges, a trend not previously accounted for with the uniform

fountain momentum flux distribution. This 2-jet fountain upwash momentum flux distribution curve was used to graphically determine  $\dot{M}_{fI_{out}}$  as:

$$\dot{M}_{fI_{out}} = \int_0^{\dot{M}_{fn_{outI}}} \frac{\dot{M}_f(\eta)}{\dot{M}_{f_{tot}}(\eta_f)} d(\dot{M}_{fn_{out}}) \quad (12)$$

Where  $\dot{M}_{fn_{out}}$  is the fountain normal momentum flux incident upon the aircraft in the outer region and  $\frac{\dot{M}_f(\eta)}{\dot{M}_{f_{tot}}(\eta_f)}$  was obtained from Figure 24.

The total fountain impingement momentum flux was then calculated as:

$$\dot{M}_{fI} = \dot{M}_{fI_{in}} + \dot{M}_{fI_{out}} \quad (13)$$

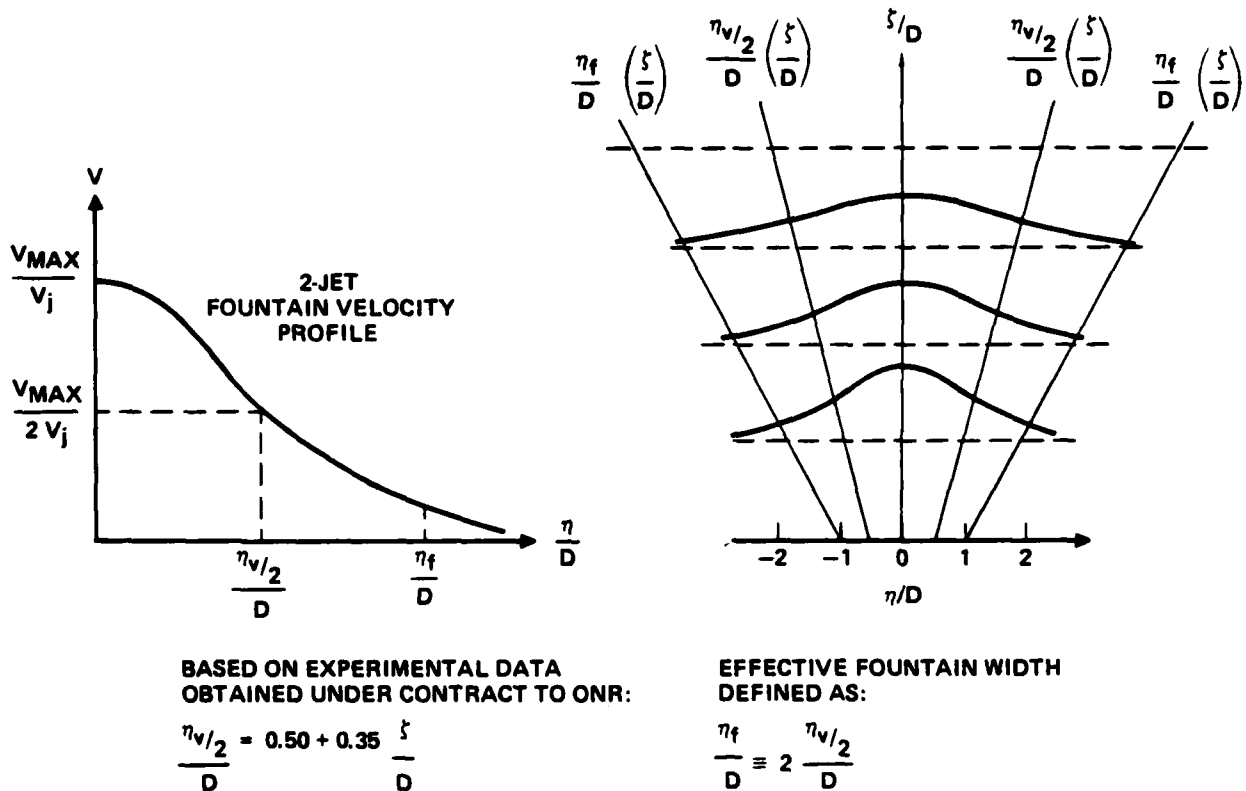


Figure 21. 2-Jet Fountain Spreading Characteristics

GP13-0002-10

NADC-81106-60

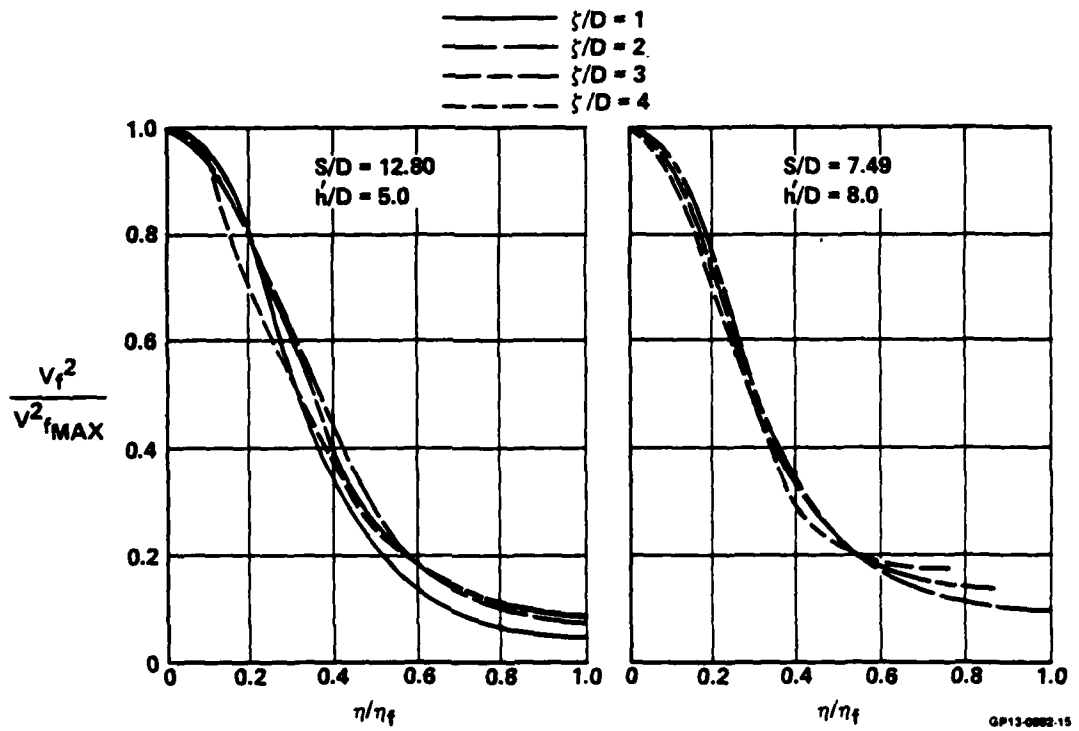


Figure 22. 2-Jet Fountain Dynamic Pressure Profiles  
Equal Thrust

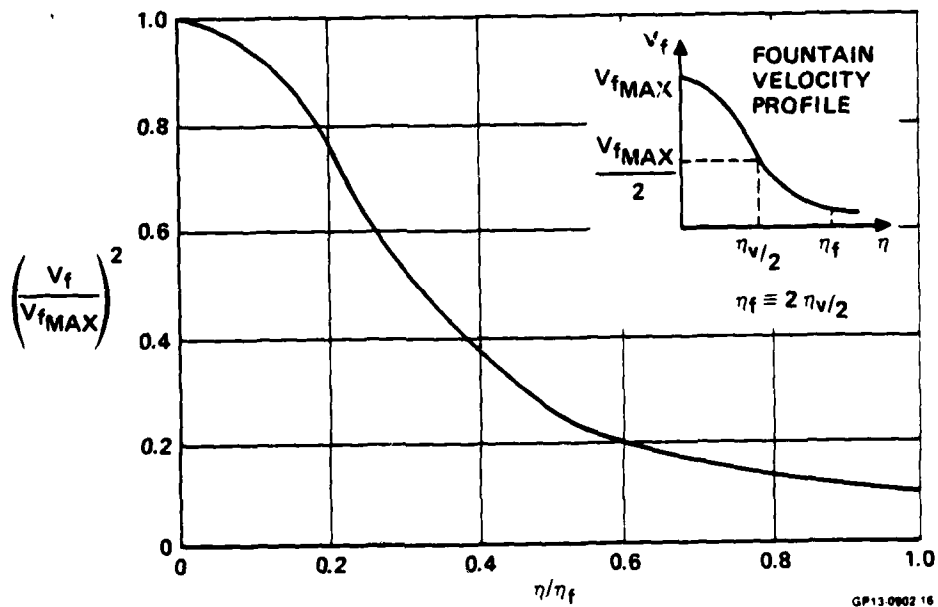


Figure 23. Empirical 2-Jet Fountain Dynamic Pressure Profile

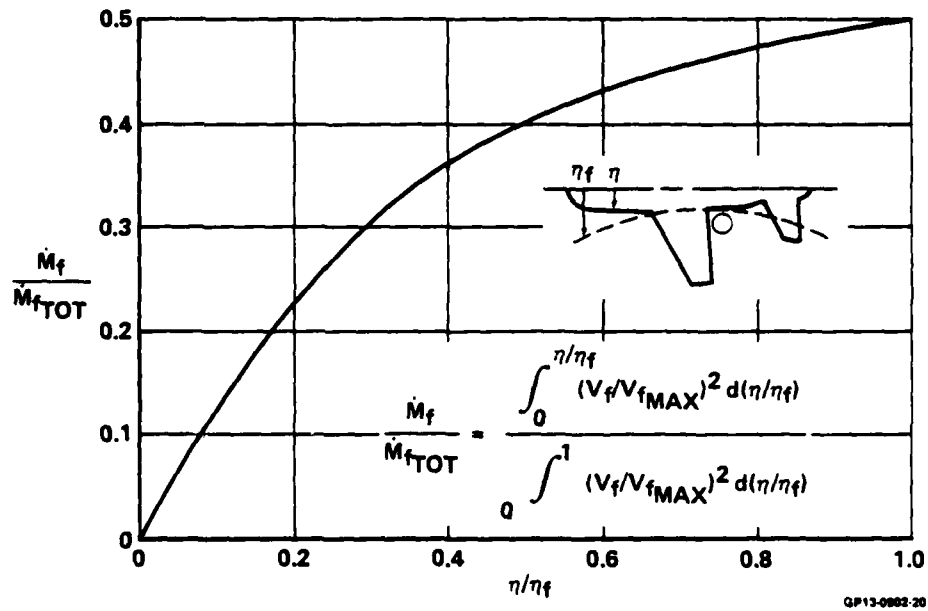


Figure 24. 2-Jet Fountain Upwash Momentum Flux Distribution

## SECTION III

CALCULATION OF  $\lambda_{fI}$ 

Using the approach described in Section II, the fountain impingement momentum flux transfer coefficient,  $\lambda_{fI}$ , was calculated for the YAV-8B, the MCAIR Model 260 and the Grumman Model 698 V/STOL aircraft at three aircraft heights above ground,  $\frac{h}{D_e}$ . The height,  $h$ , is measured normal to the ground plane surface to the point on the fuselage undersurface directly beneath the aircraft center of gravity. The diameter,  $D_e$ , is the equivalent single nozzle exit diameter defined in equation (6).

The primary quantities calculated using the MCAIR V/STOL force prediction methodology, as well as the experimentally induced lift determined for each of the aircraft configurations, are presented in Table 1. The suckdown forces, fountain impingement momentum flux magnitudes and  $\lambda_{fI}$ s calculated for the three aircraft are discussed below.

1. YAV-8B - The fountain impingement momentum flux transfer coefficient was previously determined for the YAV-8B in hover IGE at an aircraft height of  $h/D_e = 2.76$  in a related MCAIR Independent Research and Development (IRAD) study. This study was extended in the current program to include calculations of  $\lambda_{fI}$  for the YAV-8B at  $h/D_e = 1.72, 3.80$  and  $4.84$ . Figure 25 presents the paneled representation of the YAV-8B in the clean configuration without wing pylons, gun pods or fuselage strakes. The horizontal and vertical tail surfaces were assumed to contribute little to the overall suckdown force, and these surfaces were omitted from the paneled model to reduce the paneling effort and computational costs. This groundrule was adopted for the paneling of all three aircraft. For the in-ground-effect analyses, the wall jet surfaces were represented as flat, zero-thickness plates extending approximately 60 nozzle exit diameters downstream from the jet impingement points.

Unfortunately, no experimental data are available for the YAV-8B aircraft in a clean configuration (without gun pods or LID's). The fuselage contours, nozzle sizes and nozzle locations, however, are virtually identical on both the AV-8A and the YAV-8B aircraft. Consequently, the induced lift on the two aircraft was assumed to be the same, and the AV-8A data were utilized for the calculations of  $\lambda_{fI}$  for the YAV-8B in the clean configuration. Figure 26 presents the experimental data obtained for the AV-8A (from Reference 13) in the clean configuration and for the YAV-8B (from Reference 14) configured with two 16 inch fuselage strakes. Also shown in Figure 26 is the variation with height of the suckdown force,  $F_s/T$ , and the incident fountain momentum flux,  $\dot{M}_{fI}/T$ , calculated using the MCAIR V/STOL methodology. Figure 26 indicates that approximately 19% of the total jet exit momentum flux (thrust) is recovered in the fountain upwash at  $h/D_e = 1.72$  and that this value decreases to 13% at  $h/D_e = 4.84$ .

TABLE 1. CALCULATED FORCE QUANTITIES

Out of Ground Effect			
Aircraft	$\left(\frac{\Delta L}{T}\right)_{\text{exp}}$	$\frac{F_s}{T}$	$\frac{V'_{\text{fent}}}{V_{\text{fent}}}$
YAV-8B	-0.0200	-0.0044	2.132
Model 280	-0.0080*	-0.0033	1.833
Model 698	-0.0101*	-0.0003	5.491

$$\left(\frac{\Delta L}{T}\right)_{\text{exp}} = \frac{F_s}{T} + \lambda_{fl} \frac{\dot{M}_{fl}}{T}$$

\*From Byrne's correlation

In Ground Effect							
Aircraft Configuration	$\frac{h}{D_0}$	$\left(\frac{\Delta L}{T}\right)_{\text{exp}}$	$\frac{F_s}{T}$	$\frac{\dot{M}_{fl\text{in}}}{T}$	$\frac{\dot{M}_{fl\text{out}}}{T}$	$\frac{\dot{M}_{fl}}{T}$	$\lambda_{fl}$
YAV-8B without LIDs	1.72	-0.006	-0.061	0.129	0.060	0.189	0.291
	2.76	-0.006	-0.047	0.125	0.050	0.175	0.234
	3.80	-0.018	-0.039	0.107	0.041	0.148	0.142
	4.84	-0.027	-0.034	0.098	0.032	0.130	0.054
YAV-8B with LIDs	1.72	0.066	-0.061	0.129	0.060	0.189	0.672
	2.76	0.060	-0.047	0.125	0.050	0.175	0.611
	3.80	0.039	-0.039	0.107	0.041	0.148	0.527
	4.84	0.012	-0.034	0.098	0.032	0.130	0.354
Model 280 without LIDs	0.92	0	-0.048	0.064	0.031	0.095	0.505
	2.42	0.010	-0.010	0.040	0.023	0.063	0.317
	3.92	-0.009	-0.010	0.028	0.016	0.044	0.023
Model 280 with LIDs	0.92	0.033	-0.048	0.064	0.031	0.095	0.853
	2.42	0.014	-0.010	0.040	0.023	0.063	0.381
	3.92	-0.007	-0.010	0.028	0.016	0.044	0.068
Model 698 with Round Chines	0.48	-0.027	-0.037	—	0.101	0.101	0.099
	0.83	-0.015	-0.028	—	0.089	0.089	0.146
	1.89	-0.004	-0.017	—	0.064	0.064	0.203
	2.50	-0.003	-0.015	—	0.054	0.054	0.222
	3.61	-0.005	-0.012	—	0.040	0.040	0.175
Model 698 with Square Chines	0.48	-0.004	-0.037	—	0.101	0.101	0.327
	0.83	0.071	-0.028	—	0.089	0.089	1.112
	1.89	0.025	-0.017	—	0.064	0.064	0.656
	2.50	0.009	-0.015	—	0.054	0.054	0.444
	3.61	-0.005	-0.012	—	0.040	0.040	0.175

GP23-0780-21

NADC-81106-60

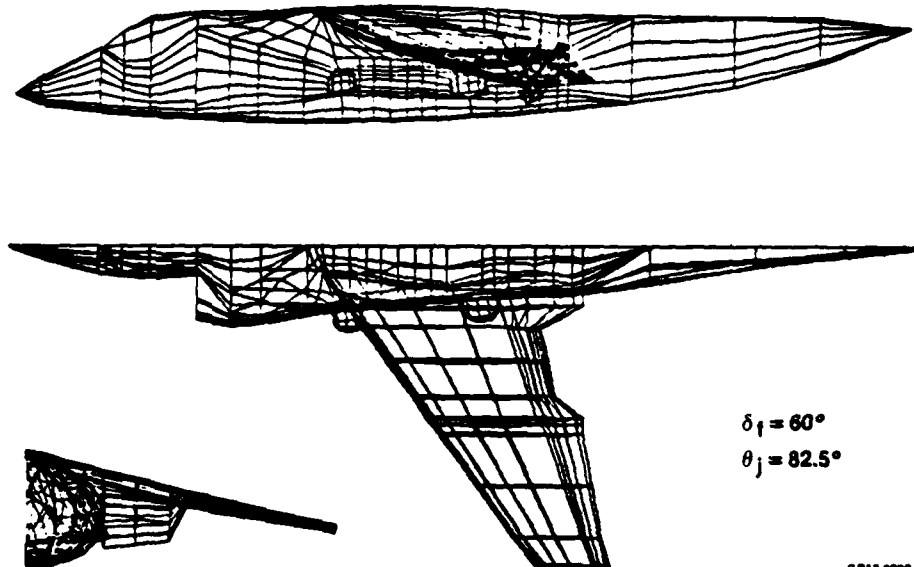


Figure 25. Paneled Representation of YAV-8B  
(Without Tail)

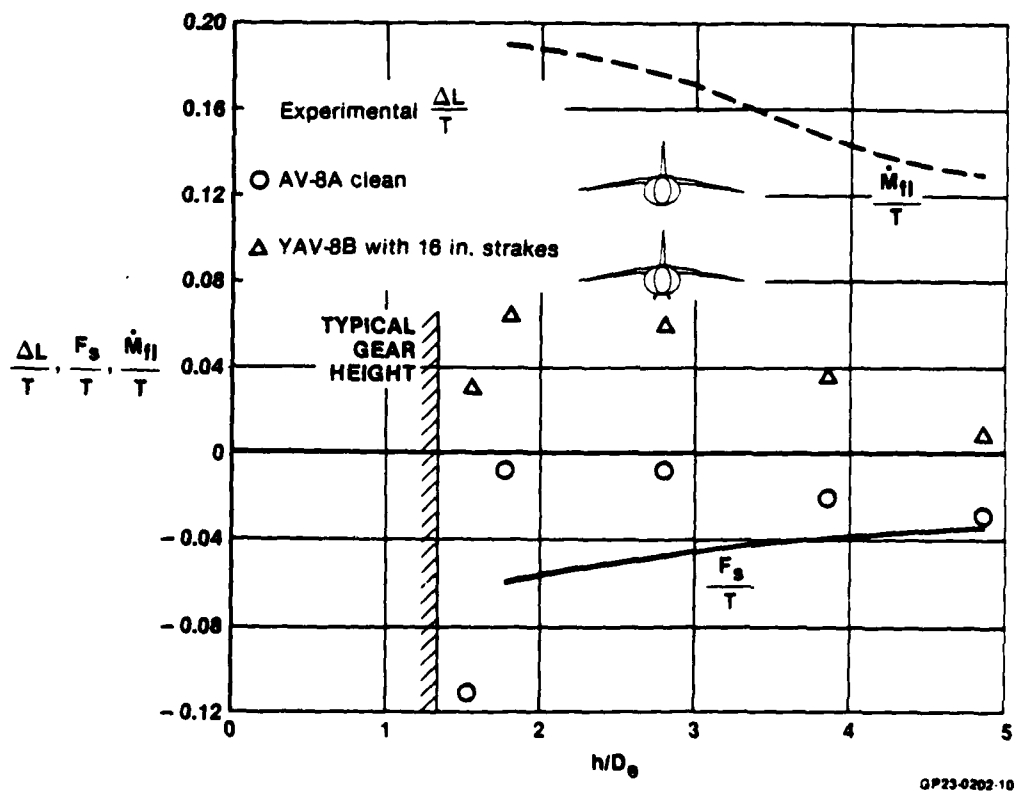


Figure 26. YAV-8B Induced Lift in Ground Effect

The fountain impingement momentum flux coefficient was calculated for the YAV-8B by rearranging equation (1) to yield:

$$\lambda_{fI} = \frac{\Delta L/T - F_s/T}{\dot{M}_{fI}/T} \quad (14)$$

Figure 27 presents the variation of  $\lambda_{fI}$  with  $h/D_e$  for the YAV-8B in both the clean configuration and with the 16 inch fuselage strakes. The presence of the strakes was assumed to have negligible effect on the calculated values of  $F_s/T$  and  $\dot{M}_{fI}/T$ . Consequently, the curves presented in Figure 26 were used to calculate  $\lambda_{fI}$  for both configurations. Figure 27 indicates that only 29% of the momentum flux within the fountain upwash is converted to a fountain impingement force on the clean configured aircraft at  $h/D_e = 1.72$ . At  $h/D_e = 4.84$ , the fountain effects are shown to be practically nonexistent on the clean aircraft with  $\lambda_{fI} = 0.05$ . The effect of adding the fuselage strakes is seen to increase the effectiveness of the fountain impingement process by capturing additionally approximately 38% of the fountain upwash momentum flux.

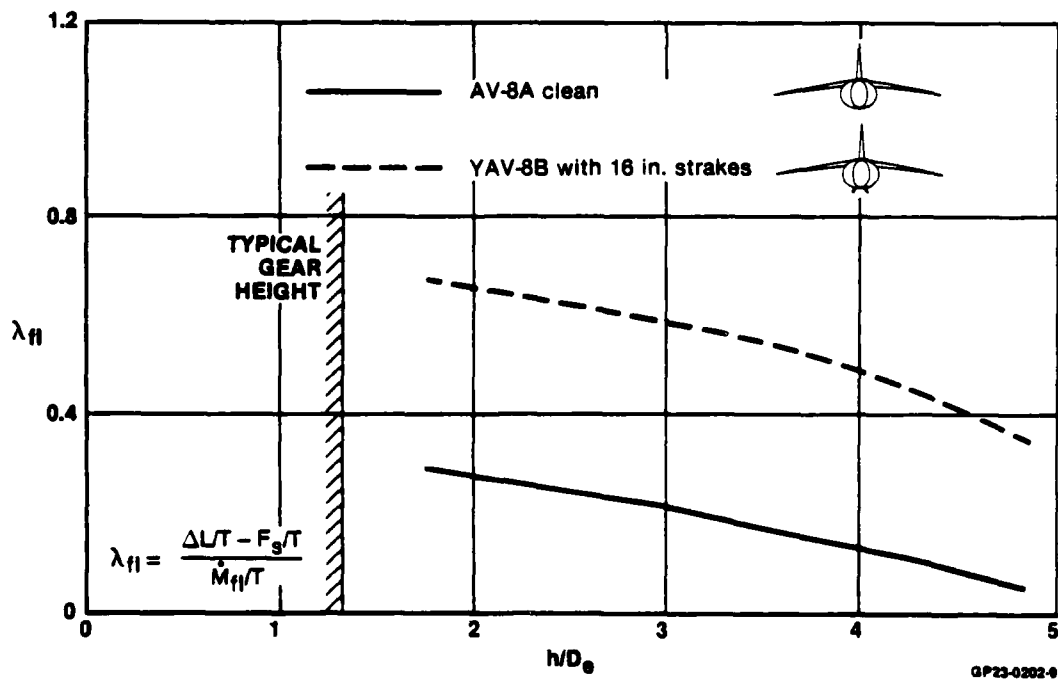


Figure 27. Fountain Impingement Momentum Flux Transfer Coefficient  
YAV-8B



2. MCAIR MODEL 260 - The fountain impingement momentum flux transfer coefficient was determined for the Model 260 aircraft at aircraft heights,  $h/D_e$ , of .92, 2.42 and 3.92. The calculations were made for the aircraft in both a clean configuration and in a configuration with lift improvement devices (LIDs) consisting of two vertical longitudinal fuselage strakes and a forward lateral vertical fence. Figure 28 presents the paneled representation of the Model 260 aircraft (without tail surfaces) in the clean, hover configuration that was utilized for the suckdown calculations. For the IGE analyses, the wall jets were again paneled as zero thickness flat plates and extended approximately 30 nozzle exit diameters downstream of the jet impingement points.

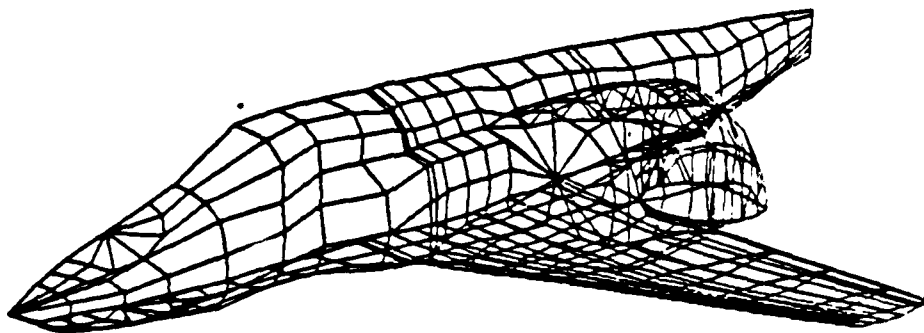
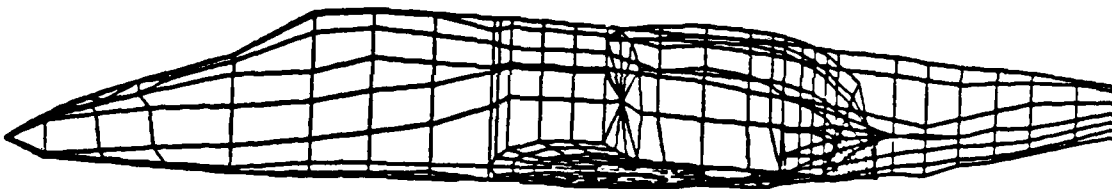
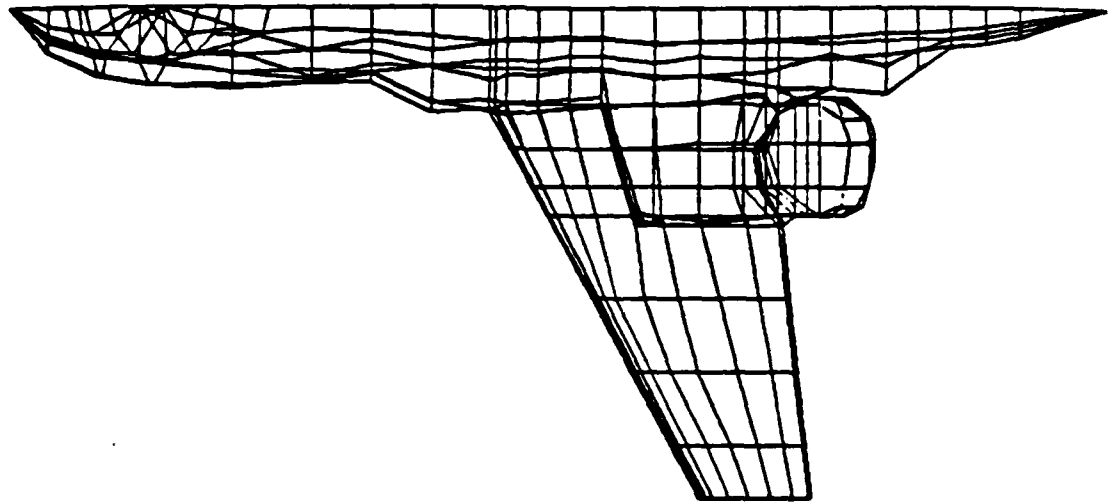
The experimentally determined induced lift ( $\Delta L/T$ ) obtained using a 4.1% scale model of the Model 260 aircraft (Reference 15), with and without LIDs, is presented in Figure 29. The data are shown for the case of all three jets impinging vertically with each jet operating at a nozzle pressure ratio of 1.50. Also shown in the figure are the calculated values of  $F_s/T$  and  $\dot{M}_{fI}/T$ . Figure 29 indicates that the Model 260 experiences approximately one third of the suckdown force as the YAV-8B and, likewise, recovers only about one third of the jet exit momentum flux in the fountain upwash.

The fountain impingement momentum flux transfer coefficients calculated for the Model 260, both with and without LIDs, are presented in Figure 30. Once again,  $\lambda_{fI}$  is found to decrease with increasing  $h/D_e$ . For the configuration without LIDs, approximately 50% of the impinging fountain momentum flux is converted to a fountain impingement force at  $h/D_e = .92$ . However, at  $h/D_e = 3.92$  only 2% of the impinging fountain upwash momentum flux is effective as a fountain impingement force. The LIDs are seen to increase the efficiency of the fountain impingement process up to an aircraft height of approximately  $2.5D_e$ . Above this height the increase in  $\lambda_{fI}$  is less than .05 over that found for the clean configuration.

3. GRUMMAN MODEL 698 - Calculations of  $\lambda_{fI}$  were made for the Grumman Model 698 aircraft at aircraft heights of  $h/D_e = .48, .83, 1.89, 2.50$  and  $3.61$ . The effect of fuselage corner radius was also investigated by examining the Model 698 with both round and square fuselage corners (or chines). Figure 31 presents the paneled representation of the Model 698 in the clean hover configuration (without vertical tail) for a nozzle exit centerline spacing ( $s/D$ ) of 2.8. The aircraft nozzles were paneled to simulate the experimental test installation.

The experimentally induced lift obtained from Reference 16 for the Model 697 with both round and square chines is presented in Figure 32. The data was obtained for the 4.2% scale model with vertically impinging jets operating at a nozzle pressure ratio of 1.06. Also shown in Figure 32 are the suckdown force,  $F_s/T$ , and the fountain momentum flux at impingement,  $\dot{M}_{fI}/T$ , calculated for the Model 698.

NADC-81106-60



GP23-0202-12

Figure 28. Paneled Representation of MCAIR Model 260

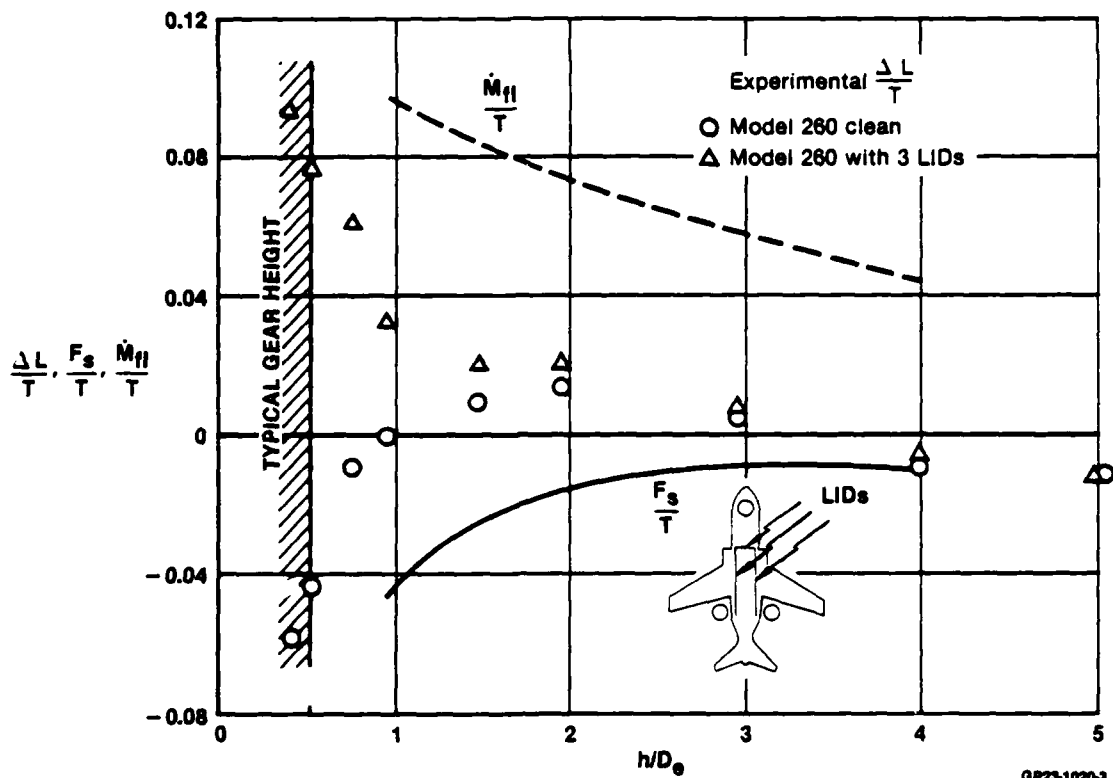


Figure 29. Model 260 Induced Lift in Ground Effect

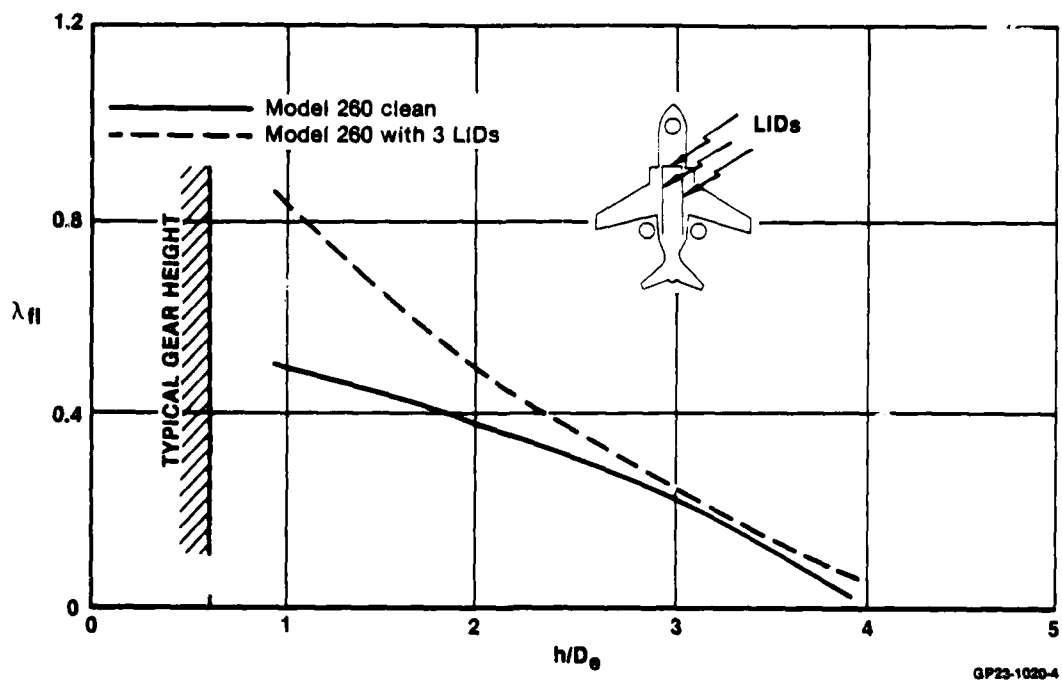
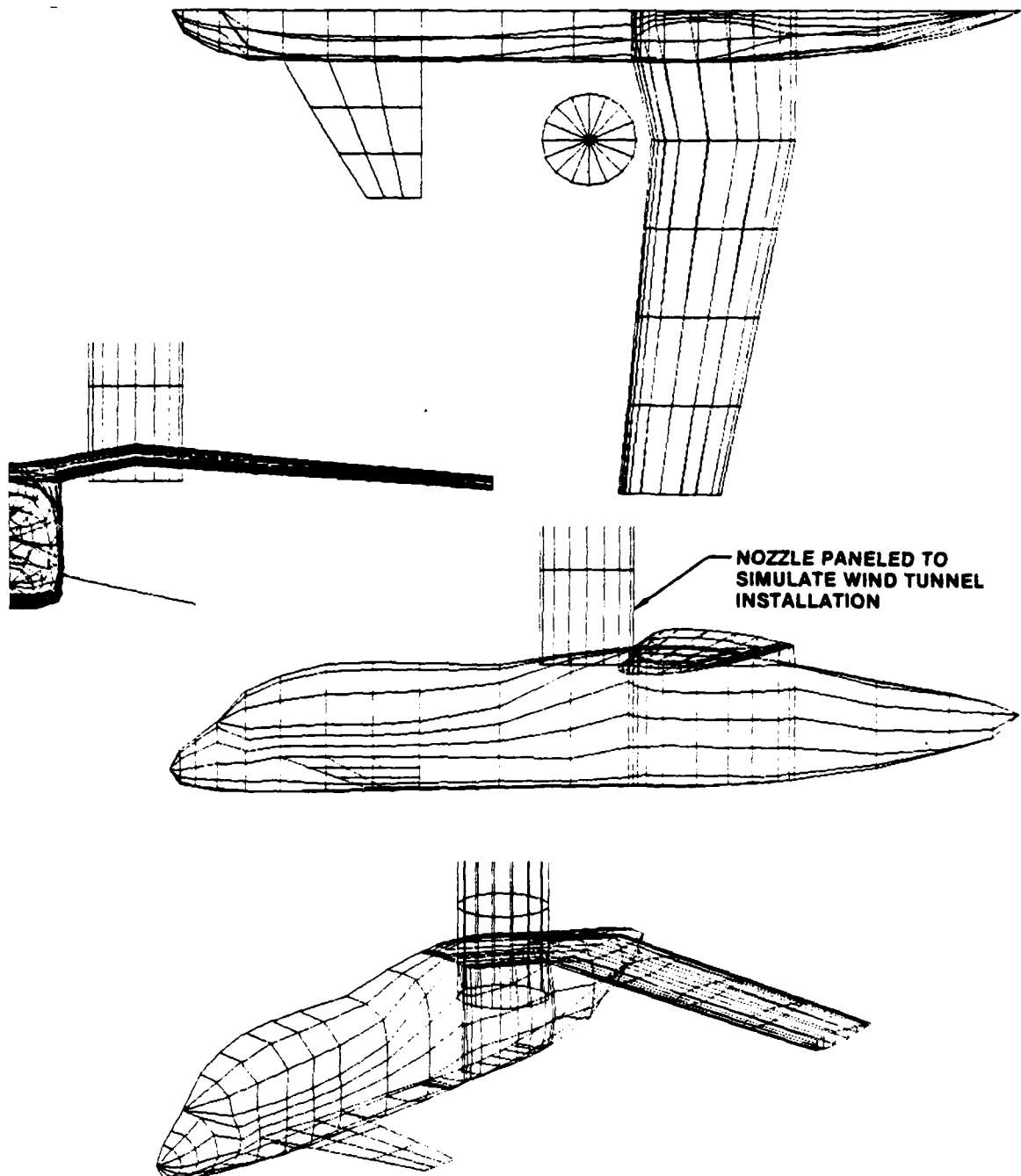


Figure 30. Fountain Impingement Momentum Flux Transfer Coefficient Model 260



GP23-0202-13

Figure 31. Paneled Representation of Grumman Model 698

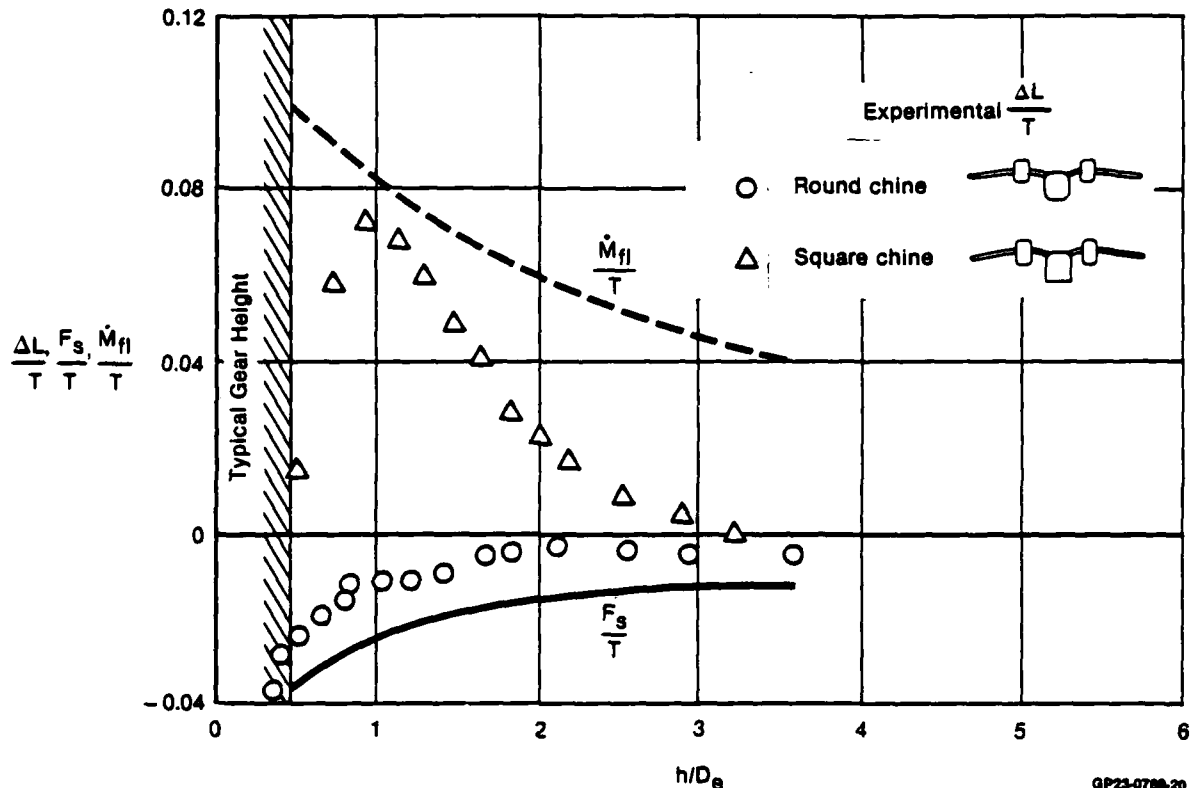


Figure 32. Grumman Model 698 Induced Lift in Ground Effect

The fountain impingement momentum flux transfer coefficients calculated for the Grumman Model 698 aircraft, with both round and square fuselage chines are shown in Figure 33. The effect of fuselage corner radius was assumed to have negligible effect on the suckdown. Consequently, the values of  $F_s/T$  and  $\dot{M}_{fI}/T$  shown in Figure 32 were utilized for both configurations to calculate  $\lambda_{fI}$ . For the aircraft with the round chines,  $\lambda_{fI}$  displays an uncharacteristic decrease with decreased  $h/D_e$  below  $h/D_e = 2.5$ . For the aircraft with the square chines,  $\lambda_{fI}$  displays the expected trend of increasing with decreasing  $h/D_e$  down to an aircraft height of  $h/D_e = .83$ . Below this height, however,  $\lambda_{fI}$  displays an unrealistic decrease in magnitude and is therefore questionable. The advantage of square chines over round chines is evident from both Figure 32 and Figure 33. A possible explanation for this effect is given by Kalemaris in Reference 16.

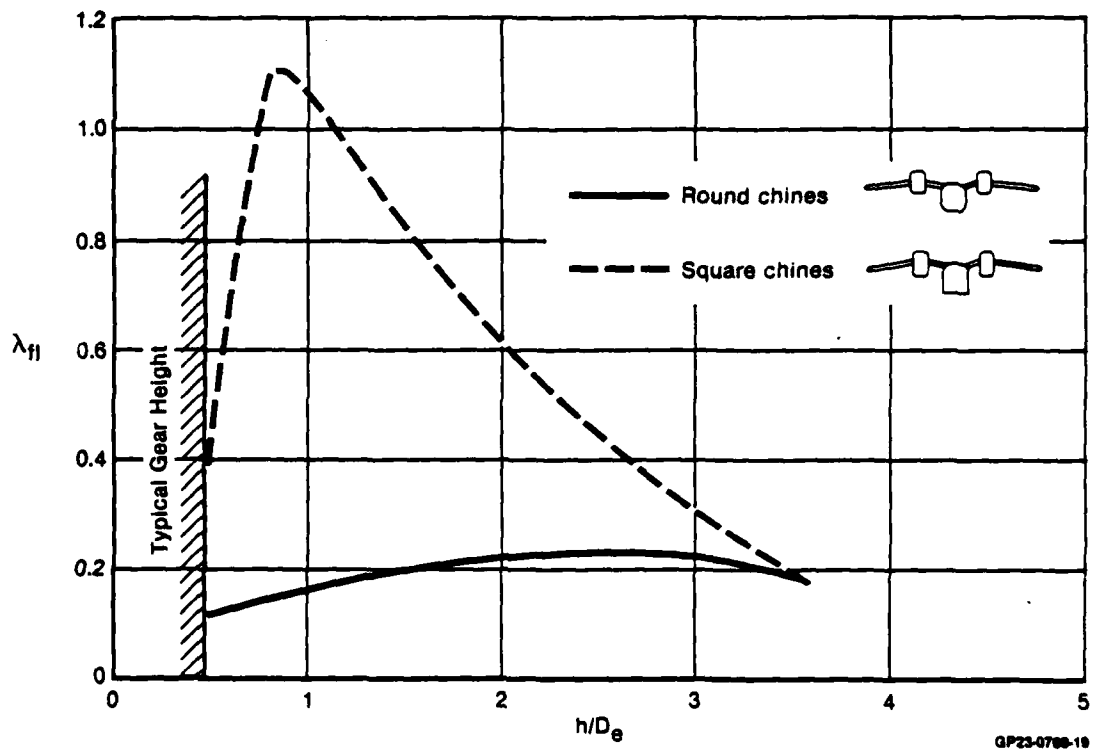


Figure 33. Fountain Impingement Momentum Flux Transfer Coefficient  
Grumman Model 698

## SECTION IV

## SUMMARY RESULTS

The fountain impingement momentum flux transfer coefficients calculated for the YAV-8B, the MCAIR Model 260 and the Grumman Model 698 aircraft are summarized in Figure 34. Since the present methodology assumes distinct regions of free jet flow, jet impingement, wall jets, fountain formation and fountain upwash; prediction of  $\lambda_{fI}$  for  $h/D_e < 1$  have been omitted from Figure 34 since distinct flow regimes do not exist at these low heights. The sensitivity of  $\lambda_{fI}$  due to fuselage undersurface shape is apparent by comparing the curves in Figure 34 for the YAV-8B with and without LIDs. This sensitivity is also displayed by the Model 260 and the Model 698 at the lower aircraft heights where significant fountain capture exists.

The fuselage cross-sections associated with the Model 260 and the Model 698 aircraft are in general quite similar, displaying a flat bottom with rounded corners. The YAV-8B fuselage, on the other hand is rounded across the entire width. However, the fountain impingement momentum flux coefficients calculated for the Model 260 (without LID's) are quite similar to those determined for the YAV-8B (without LID's), while the  $\lambda_{fI}$ s calculated for the Model 698 (with round chines) were much lower. This suggests that the  $\lambda_{fI}$  associated with multiple jet V/STOL aircraft producing a central fountain may be fundamentally different from those associated with 2-jet V/STOL aircraft where no central fountain is formed.

Figure 34 also illustrates the dependence of  $\lambda_{fI}$  on  $h/D_e$ , with  $\lambda_{fI}$  decreasing with increased aircraft height.  $\lambda_{fI}$  was originally expected to be relatively insensitive to variations in  $h/D_e$  providing the fountain upwash was adequately modeled. The  $h/D_e$  dependency illustrated in Figure 34 may thus be a result of inadequate fountain modeling. This inaccuracy may result from one of two identified problem areas: (1) insufficient empirical data defining central fountain core upwash characteristics, and/or (2) lack of an adequate model defining conditions for, and magnitude of, fountain upwash interaction with the downward impinging jet flows. (The characteristics of four-jet central fountains were investigated in a MCAIR Independent Research and Development experimental program in 1982.) The utility of the MCAIR V/STOL force prediction methodology, however, is not severely impaired by the absence of these fountain models since inadequacies associated with the fountain upwash models are inherently accounted for in  $\lambda_{fI}$ .

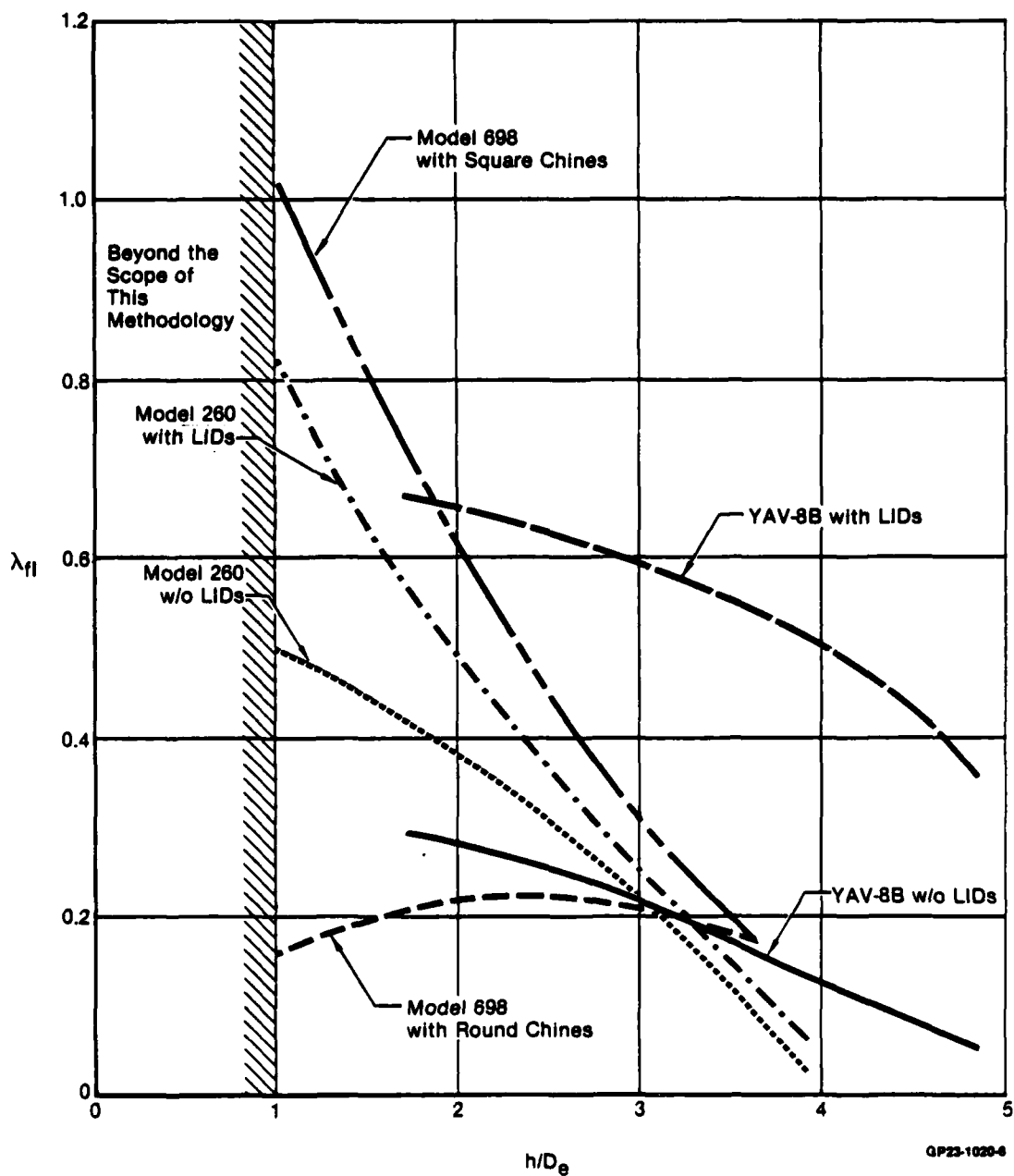


Figure 34. Fountain Impingement Momentum Flux Transfer Coefficient Summary



The agreement between the indirect and direct methods of measuring mass entrainment discussed in the Appendix and shown in Figure A13 indicates that both approaches are accurate. Although the entrainment rates determined in this study are higher than those determined previously (Figure A1), the difference is still too small to account for the magnitude of the suckdown forces reported in Section II.1.a\*.

\*The suckdown force on the Model 698 aircraft out-of-ground effect was recalculated using the entrainment rates determined for nozzle A at NPR = 1.10 ( $m_1 = .334$ ,  $m_2 = .422$ ) as  $\frac{\Delta L}{T} = -.0008$ . This may be compared with the semi-empirical value of  $\frac{\Delta L}{T} = -.0101$  determined using Byrne's formula (Figure 10).

## SECTION V

## CONCLUSIONS

Based on the calculations of the suckdown force determined for the MCAIR YAV-8B, the MCAIR Model 260 and the Grumman Model 698 in hover out of ground effect, it was concluded that existing empirical free jet entrainment rates are too weak. The results of the experimental investigation of free jet mass entrainment validate the indirect method and indicate that the indirect method may be applied to situations in which use of the direct method may be impractical. Three such situations are depicted in Figure 35. The first situation represents the case of a high velocity jet in which the flow dynamics would be too severe for penetration with a standard hot film probe. The second situation is that of two or more merging jets. In this case, distinct free jet velocity profiles may not be attainable or the required survey volume may be too large for use of the direct method. The final situation represents the case of a very hot jet in which immersion by standard probes may not be practical.

The  $\lambda_{fj}$ s determined for the three aircraft using the MCAIR hover methodology with adjusted free jet and wall jet mass entrainment rates indicated a general trend, with  $\lambda_{fj}$  decreasing with increased aircraft height above ground. Use of additional lift jets decreases the rate of decay of  $\lambda_{fj}$  with aircraft height.

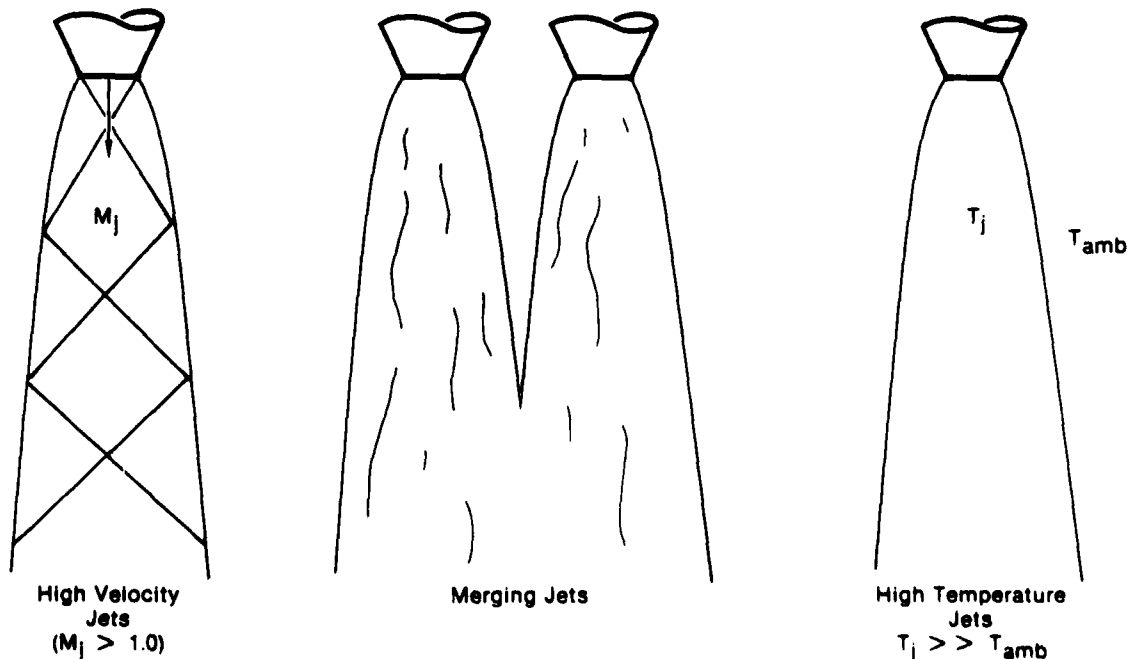


Figure 35. Potential Applications of the Indirect Method of Determining Free-Jet Mass Entrainment

GP23-0700-2

REFERENCES

1. Kotansky, D.R., Durando, N.A., Bristow, D.R., and Saunders, P.W., "Multi-Jet Induced Forces and Moments on VTOL Aircraft Hovering In and Out of Ground Effect", Final Technical Report, Naval Air Development Center, NADC Report No. 77-229-30, June 1977.
2. Kotansky, D.R., and Glaze, L.W., "Investigation of Impingement Region and Wall Jets Formed by the Interaction of High Aspect Ratio Lift Jets and A Ground Plane", Report No. NASA CR 152174, Ames Research Center, 19 September 1978.
3. Kotansky, D.R., and Glaze, L.W., "Investigation of the Interaction of Lift Jets and a Ground Plane", Report No. NASA CR 152343, Ames Research Center, April 1980.
4. Glaze, L.W., "KCCX-Aircraft/Ground/Stagnation Line/Fountain (AGSF) Computer Program User's Manual", Report MDC A6635, McDonnell Aircraft Company, 10 October 1980.
5. Kotansky, D.R., and Glaze, L.W., "The Effects of Ground Wall Jet Characteristics on Fountain Upwash Flow Formation and Development", Report No. ONR-CR212-261-1F, Office of Naval Research, 15 June 1980.
6. Moran, J., Tinoco, E.N., and Johnson, F.T., "User's Manual Subsonic/Supersonic Advanced Panel Pilot Code", NASA CR-152047, Ames Research Center, February 1978.
7. Hill, B.J., "Measurement of Local Entrainment Rate in the Initial Region of Axisymmetric Turbulent Air Jets", Journal of Fluid Mechanics, Vol. 51, Part 4, pp 773-779, 1972.
8. Kleis, S.J., and Foss, J.F., "The Effect of Exit Conditions on the Development of an Axisymmetric Turbulent Free Jet", Third Year Technical Report, NASA Grant NGR 23-004-068, Michigan State University, 15 May 1974.
9. Ricou, F.P., and Spalding, D.B., "Measurements of Entrainment by Axisymmetric Turbulent Jets", Journal of Fluid Mechanics, Vol. 11, Part 1, p. 21, 1961.
10. Wagnanski, I., "The Flow Induced by Two-Dimensional and Axisymmetric Turbulent Jets Issuing Normally to an Infinite Plane Surface", Report No. 63-12, Mechanical Engineering Research Laboratories, McGill University, Montreal, Canada, December 1963.
11. Trentacoste, N., and Sforza, P., "Further Experimental Results for Three-Dimensional Free Jets", AIAA Journal, Vol. 5, No. 5, p. 885, May 1967.

12. Henderson, C., Clark, J., and Walters, M., "V/STOL Aerodynamics and Stability and Control Manual", Report No. NADC-80017-60, Naval Air Systems Command, P. 2.2.1-7, 15 January 1980.
13. Lacey, T.R., "AV-8A 15% Scale-Powered Mini and Low Speed Wind Tunnel Program", Volume 1, McDonnell Douglas Corporation A3207, 25 February 1975.
14. "YAV-8B Aerodynamic Stability and Control and Flying Qualities", McDonnell Douglas Corporation A4637, January 1980.
15. Kamman, J.H. and Hall, C.L., "Lift System Induced Aerodynamics of V/STOL Aircraft in a Moving Deck Environment", Volume I, NADC-77-107-30, Naval Air Development Center, 26 September 1978.
16. Kalemari, S.G., "Evaluation of the Effects of Model Scale and Test Technique on Jet Induced Effects". From AGARD-CP-308, Proceedings of Fluid Dynamics of Jets with Application to V/STOL, January 1982.

## APPENDIX A

During the study described in the preceding sections, it was determined that existing empirical axisymmetric free jet entrainment rates (Figure A1) are too low for the accurate prediction of suckdown forces on V/STOL aircraft in hover. The conventional experimental approach for determining the entrained mass distribution is based upon detailed velocity measurements within the jet. If the axial velocity component is measured at enough points on a cross-section to establish a velocity profile, then the local mass flux can be determined by integration. The accuracy of this direct approach, however, is highly sensitive to the accuracy of the probe sensor and survey position calibration and to the numerical integration method selected. As an alternative to this approach, MCAIR developed a new technique to indirectly measure the entrainment rates associated with axisymmetric free jets. This indirect method was developed as a means of validating the direct approach and to verify the potential flow model of jet entrainment induced flowfields. The indirect method utilizes a hot film anemometer (HFA) to measure the induced velocity field about subsonic, axisymmetric free jets. Inverse potential flow theory is employed to convert the measured induced velocities to mass entrainment rates. This technique was applied in an experimental program by MCAIR in order to quantify the dependence of free jet mass entrainment on nozzle pressure ratio and turbulence intensity for isolated subsonic axisymmetric jets. The technical approach, experimental test program and test results are described in the following sections.

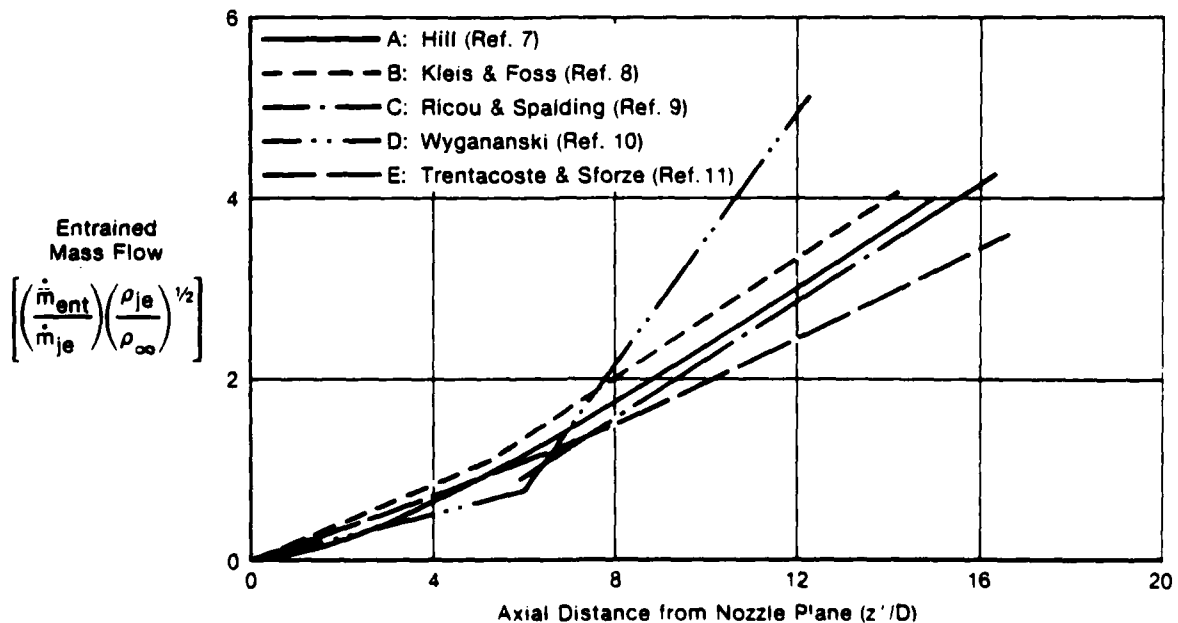
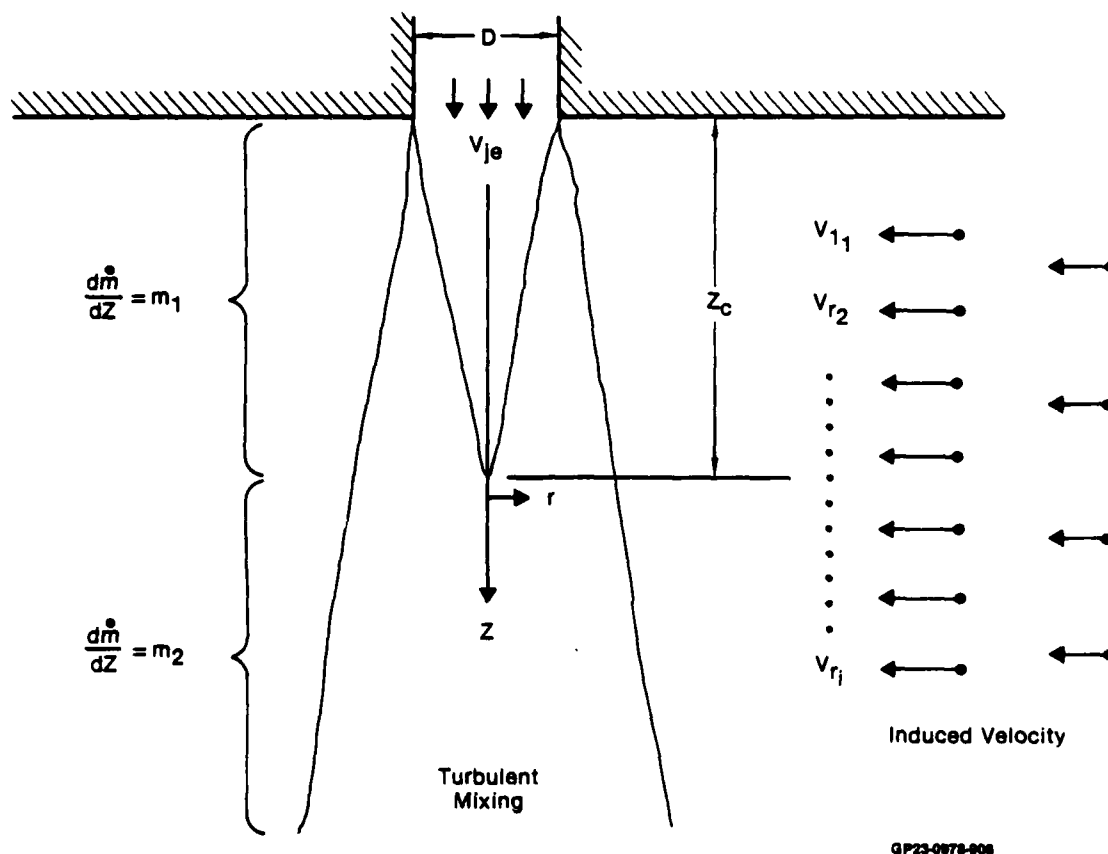


Figure A1. Entrained Mass Flow Distribution for Circular Jets

**A.1 TECHNICAL APPROACH** - Consider a set of  $n$  points outside of the mixing region of a jet (Figure A2). Suppose that at each point  $(z_i, r_i)$ , the radial velocity component  $V_r$  has been measured experimentally. The data reduction procedure described below will determine the jet entrained mass distribution that most nearly corresponds to the measured velocity field, in the sense of a least square error.



GP23-0978-008

**Figure A2. Representation of an Axisymmetric Subsonic Jet for Indirect Mass Entrainment Measurements**

The mechanism for converting measured velocity to mass entrainment is inverse potential flow theory. It is assumed that the jet can be represented by a potential core region of length  $z_c$  and a semi-infinite fully developed region (Figure A2). Prior investigations have shown  $z_c$  to be approximately equal to six nozzle exit diameters ( $z_c = 6D$ ). The rate of mass entrainment per unit length ( $dm/dz$ ) is assumed to be an unknown constant  $m_1$  in the potential core region and a second unknown constant  $m_2$  in the fully developed region. If the values  $m_1$  and  $m_2$  were known a priori, the calculation of induced radial velocity component  $V_r$  at any point  $(z, r)$  would be straightforward. The jet would be represented by a distribution of sinks along the centerline, where the sink strength would be  $m_1$  in the potential core region

( $0 < z < z_c$ ) and  $m_2$  in the fully developed region. Image sinks for  $z < 0$  would simulate the presence of the flat exit plane at  $z = 0$ . The formula for  $V_r$  is:

$$V_r(z, r) = \frac{m_2}{2\pi r \rho} + \frac{m_1 - m_2}{4\pi r \rho} \left[ \frac{(z + z_c)}{\sqrt{r^2 + (z + z_c)^2}} - \frac{(z - z_c)}{\sqrt{r^2 + (z - z_c)^2}} \right] \quad (A1)$$

where the density  $\rho$  is constant in low speed flow.

Here it is desired to solve for the unknowns  $m_1$  and  $m_2$  such that  $V_r(z, r)$  from equation (A1) will approximately match the experimentally measured value  $V_{ri}$  at each of the probe positions  $(z_i, r_i)$ . Formally, the objective is to minimize the quadratic error function.

$$E = \sum_{i=1}^n \left[ \frac{V_r(z_i, r_i) - V_{ri}}{V_{ri}} \right]^2 \quad (A2)$$

The minimization of  $E$  is accomplished by substituting (A1) into (A2) and differentiating (A2) with respect to the two unknowns. This results in a system of two equations which may be solved directly for  $m_1$  and  $m_2$ . Following the determination of  $m_1$  and  $m_2$  the entrained mass distribution can be expressed as

$$m = \begin{cases} m_1 z & 0 < z < z_c \\ (m_1 - m_2) z_c + m_2 z & z_c < z \end{cases} \quad (A3)$$

**A.2 EXPERIMENTAL TEST PROGRAM** - The experimental test program was conducted in the Inlet Simulator test cell of the MCAIR Propulsion Subsystem Test Facility (PSTF). The facility utilizes high pressure (4137 kPa) air from the air storage system of the MCAIR Polysonic Wind Tunnel. The experimental program was designed to provide accurate measurements of the mass entrainment induced by an axisymmetric free jet for parametric variations in nozzle pressure ratio (NPR) and free jet turbulence intensity levels. The experimental test hardware, test procedure and results are described below.

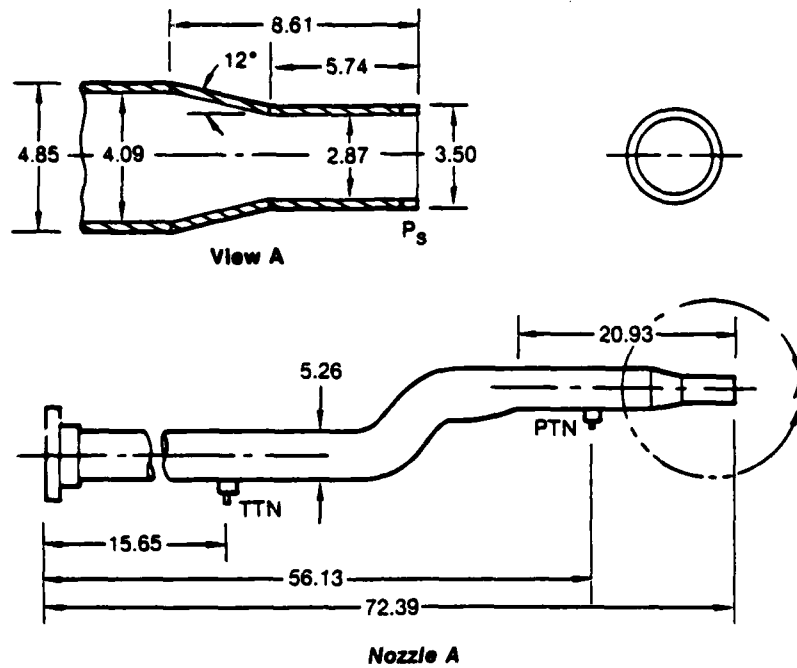
**A.2.1 Test Hardware and Instrumentation** - Two existing converging nozzle pipes were used for the test program. These nozzles, designated nozzle A and nozzle B, are illustrated in Figure A3. Nozzle A, which was used for the investigation of nozzle pressure ratio effects, has a nozzle exit diameter ( $D_A$ ) of 2.87 cm. Nozzle B was used for the investigation of turbulence effects and has a nozzle exit diameter ( $D_B$ ) of 5.90 cm. Each of the nozzles is instrumented with four (4) nozzle exit static pressure taps, one (1) total pressure probe and one (1) total temperature probe. In addition, nozzle B is constructed such that a series of turbulence generating plates and screens may be

inserted in the nozzle pipe at a distance of  $3.23 D_B$  (19.05 cm) upstream of the nozzle exit plane. Substantial effort was spent to determine the most suitable combinations of plates and screens for producing turbulence levels different from that of the baseline nozzle configuration and, at the same time, yielding a symmetrical jet. The final nozzle configurations utilized for the turbulence effects investigation are designated T0, T7 and T8. Nozzle configuration T0 is the baseline configuration and consists of nozzle B with no internal plates or screens. Nozzle configuration T7 consists of the baseline configuration with the addition of a perforated plate upstream of the nozzle exit. Nozzle configuration T8 is represented by the T7 nozzle assembly with a screen (T5) installed directly downstream of the perforated plate. The T7 plate and the T5 screen utilized for configuration T8 are illustrated schematically in Figure A4.

A 127.0 cm diameter circular nozzle exit plane plate was fabricated from plexiglass for the test. Provisions were made to enable the attachment of a remotely controlled single degree-of-freedom probe traverse device to the back of the plate such that the hot film anemometer probe could be traversed in a direction normal to the plate surface at any one of nine radial locations. The nozzle exit plane plate was adaptable for use with either nozzle A or nozzle B.

Free jet mean velocity ( $\bar{U}$ ) and turbulence intensity ( $u'/\bar{U}$ ) levels were established using a single sensor TSI Model 1213-20 hot film anemometer probe. The jet entrainment induced velocity field surrounding the axisymmetric jet was mapped out using a specially designed TSI Model 1330XX temperature compensated hot film probe (Figure A5). In order to maximize the sensitivity of the probe to the radial inflow, the hot film sensor was placed on the upstream side of the probe only. In addition, since the hot film probe is primarily sensitive to the velocity component normal to the sensor axis, the probe was oriented such that the sensor axis was parallel to the free jet centerline. The hot film probes were calibrated using a TSI Model 1125 calibrator with an accuracy of  $\pm 1.0\%$  for velocities above 3.0 m/sec and with an accuracy of  $\pm 2.0\%$  for a velocity range of .15 m/sec - 3.0 m/sec. The RMS value of the fluctuating portion of the free jet velocities ( $u'$ ) were determined using a Ballantine Model 323 true RMS meter. The free jet nozzle exit velocity profiles were determined using a United Sensors Model PRC-18-C-16-KL pitot-static pressure probe.





Note: All dimensions in cm

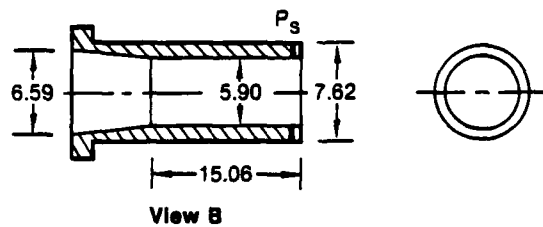
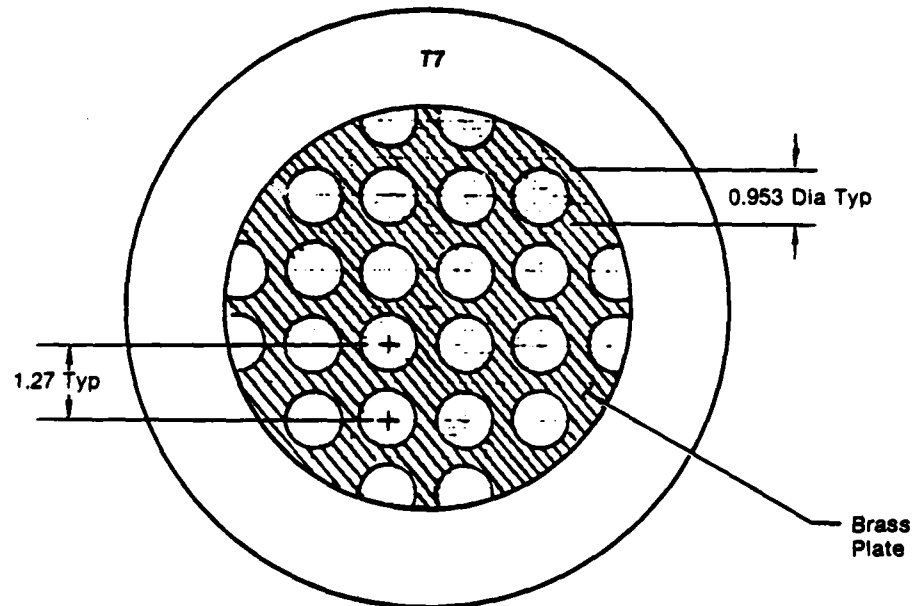
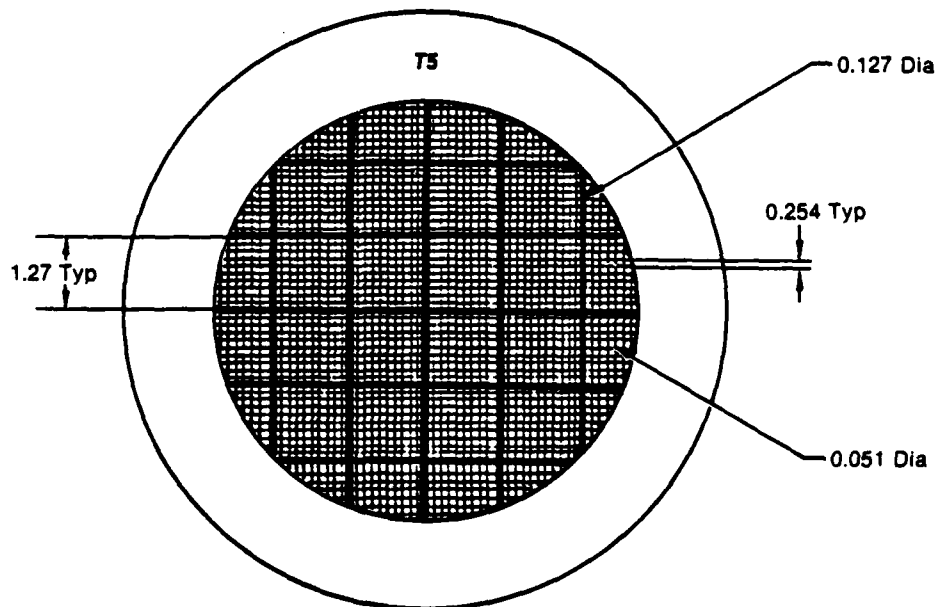


Figure A3. Baseline Nozzle Configurations

GP23-0788-17

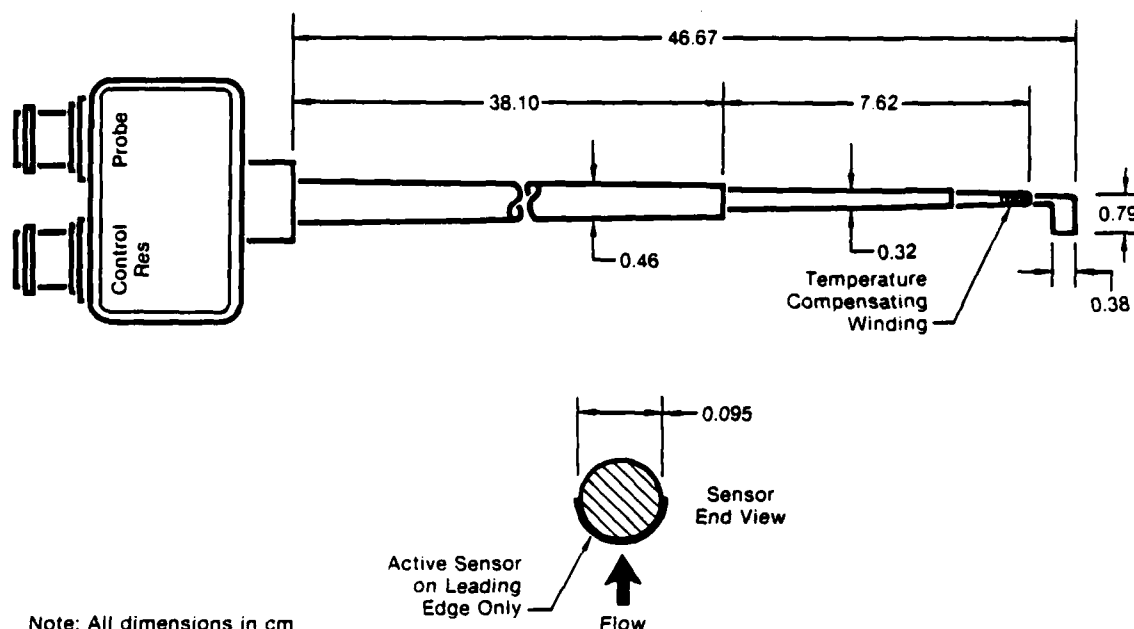


Note: All dimensions in cm



GP23-0788-14

Figure A4. Turbulence Generators



Note: All dimensions in cm

GP23-0700-16

Figure A5. TSI Model 1330XX Temperature Compensated Hot Film Anemometer Probe

**A.2.2 Test Procedure** - The experimental test program is outlined in Table A1. Nozzle exit velocity profile surveys were performed to investigate the uniformity and symmetry of the nozzle exit flow. Figure A6 presents the nozzle exit velocity profiles obtained for nozzle A at NPR = 1.10, 1.35 and 1.80. The velocity  $U$  is normalized by the jet centerline velocity ( $U_{CL}$ ) obtained at  $y = 0$ . Figure A6 illustrates that the nozzle exit flow was relatively uniform (within 2% of  $U_{CL}$ ) for all three nozzle pressure ratios except near the edge of the jet where viscous effects occur. The effect of the turbulence generators on the velocity profile generated by nozzle B at NPR = 1.10 is illustrated in Figure A7. The baseline nozzle (T0) displays a uniform, symmetrical "top hat" profile. Addition of the T7 plate accelerated the flow at the edge of the jet to approximately  $1.22 U_{CL}$ . Addition of the T5 screen downstream of the T7 plate (configuration T8) smoothed out the peaks somewhat, but still produced flow at the edge of the jet that was approximately 8% higher than  $U_{CL}$ .

The turbulence intensity ( $\frac{u'}{U}$ ) of the jets was determined for NPR = 1.10 using the hot film anemometer to simultaneously measure the root mean square of the fluctuating axial velocity ( $u'$ ) and the mean axial velocity ( $\bar{U}$ ). (Extreme flow dynamics prevented use of the delicate hot film anemometer sensor for nozzle A at the higher NPRs.) The free jet mean axial velocity profiles and turbulence intensity profiles obtained for nozzle B in the T0, T7 and

m8 configurations at  $\text{NPR} = 1.10$  and  $z/D_B = 1.0$  are presented in Figure A8. X-Y-Y plotter tracings of the HFA output voltages were used to interpolate between data points on the mean velocity profile.

TABLE AI. TEST PROGRAM

**Exit Velocity Profile Surveys**

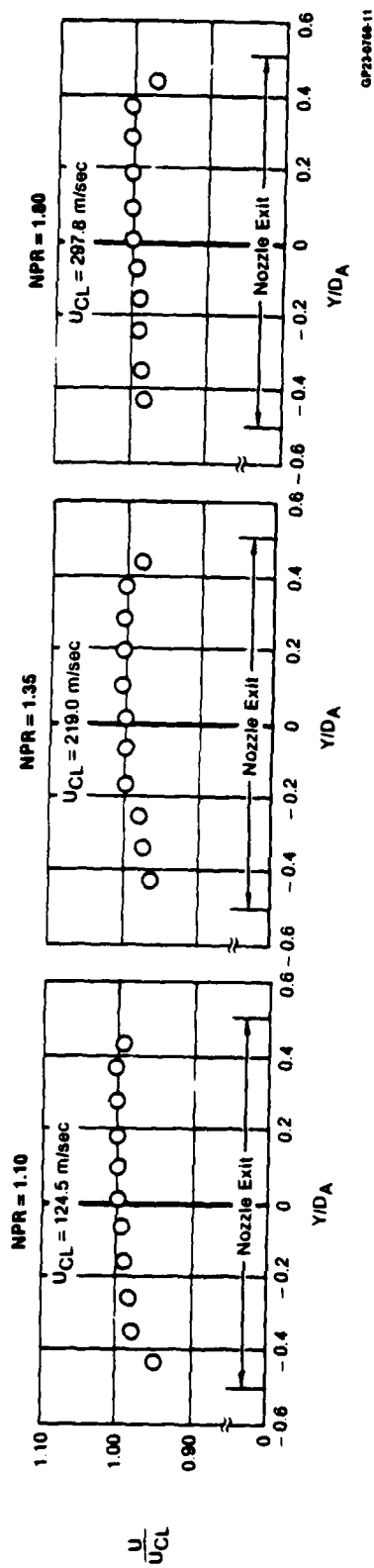
- Nozzle A
  - $\text{NPR} = 1.10, 1.35, 1.80$
  - $Z/D_A = 0.04$
  - $Y/D_A = -0.43, -0.35, -0.26, -0.18, -0.08, 0, 0.09, 0.18, 0.27, 0.36, 0.42$
- Nozzle B
  - $\text{NPR} = 1.10$
  - Turbulence Generator: T0, T7, T8
  - $Z/D_B = 0.02$
  - $Y/D_B = -0.47, -0.43, -0.35, -0.26, -0.17, -0.08, 0, 0.09, 0.17, 0.26, 0.35, 0.44, 0.47$

**Turbulence Intensity Surveys**

- Nozzle A
  - $\text{NPR} = 1.10$
  - $Z/D_A = 1.0, 2.0, 4.0, 6.0, 9.0, 12.0$
- Nozzle B
  - $\text{NPR} = 1.10$
  - Turbulence Generator: T0, T7, T8
  - $Z/D_B = 1.0, 2.0, 4.0, 6.0, 9.0$

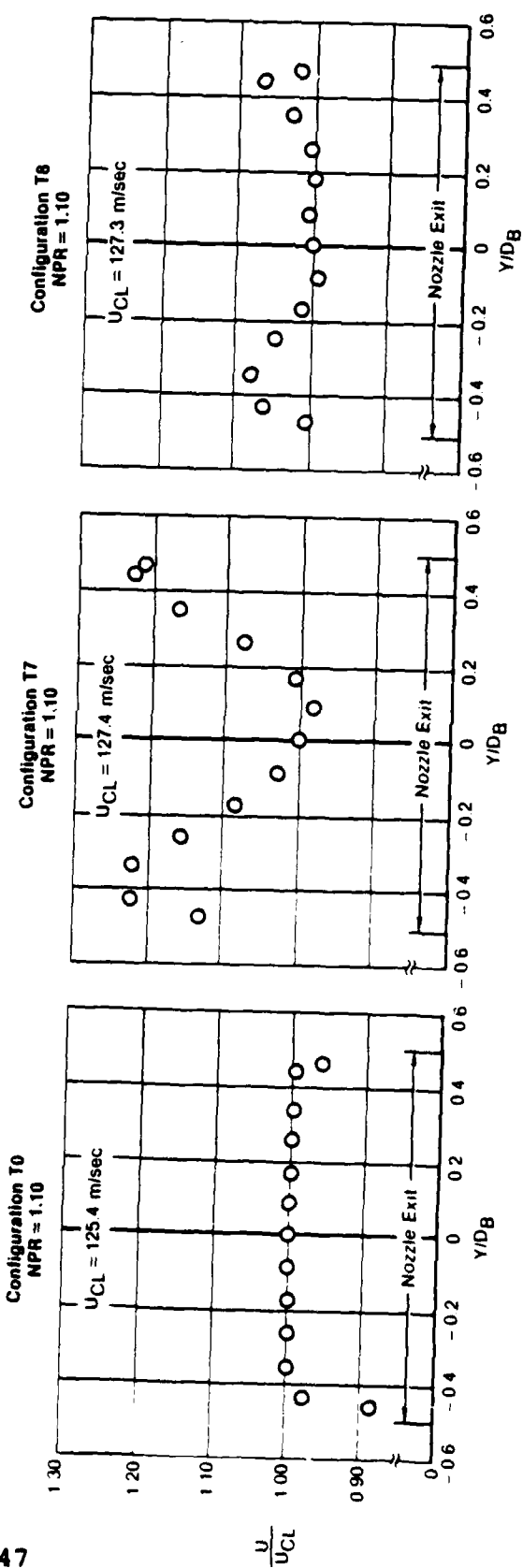
**Entrainment Velocity Measurements**

- Nozzle Pressure Ratio Effects
  - Nozzle A
    - $\text{NPR} = 1.10, 1.35, 1.80$
    - $R/D_A = 4.0, 5.0, 6.0, 7.0, 8.0, 10.0, 12.0$
    - $Z/D_A = 0.5, 1.0, 2.0, 3.0, 4.0, 6.0, 8.5, 11.0$
    - $\phi = 0^\circ, 180^\circ, 270^\circ$
- Turbulence Effects
  - Nozzle B
    - $\text{NPR} = 1.10$
    - Turbulence Generator: T0, T7, T8
    - $R/D_B = 2.913, 3.885, 4.856, 5.827, 7.284, 9.225$
    - $Z/D_B = 0.5, 1.0, 2.0, 3.0, 4.0, 5.5$
    - $\phi = 0^\circ, 180^\circ, 270^\circ$



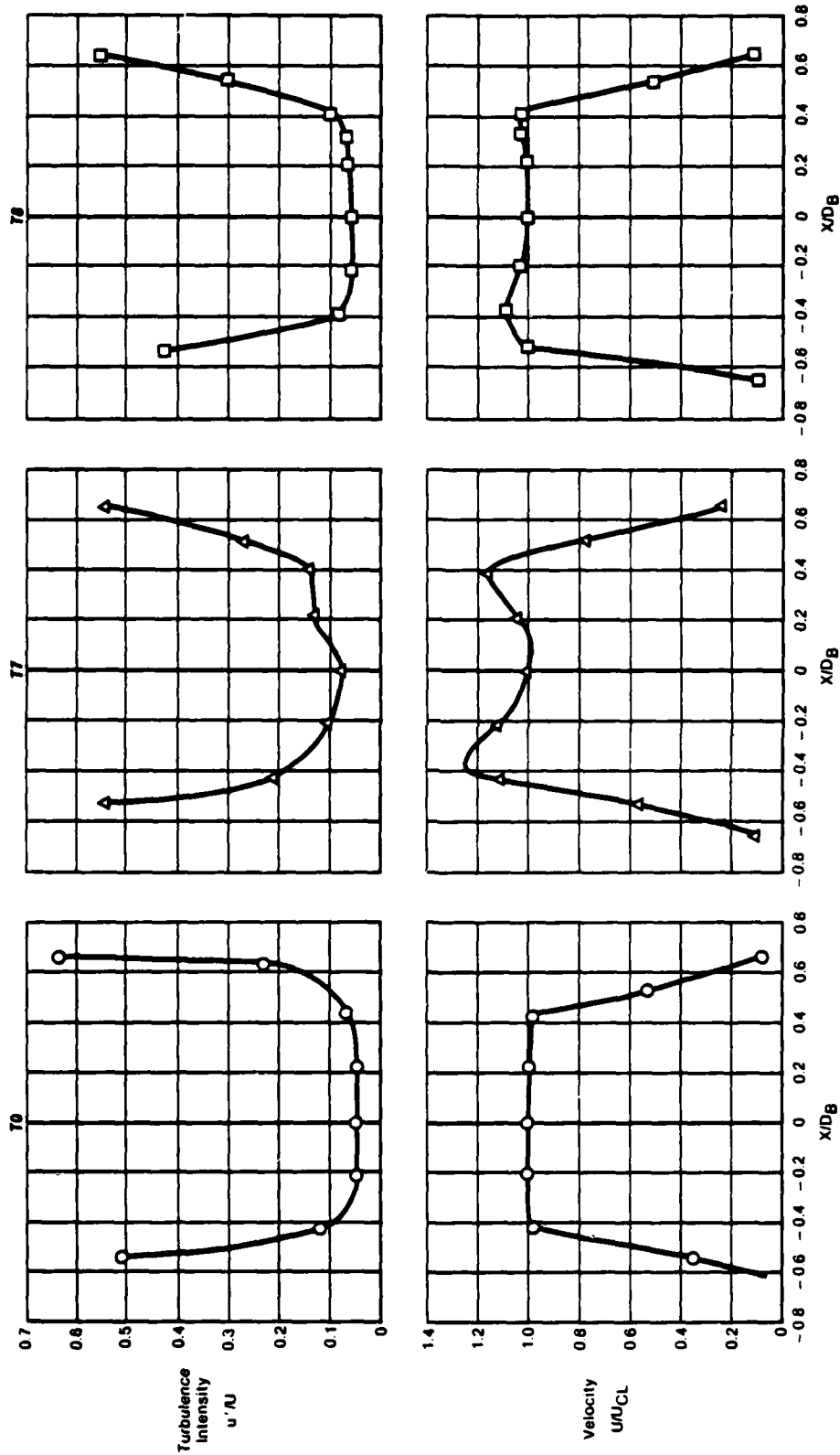
GP23-8746-11

Figure A6. Nozzle Exit Plane Velocity Profiles  
Nozzle A



GP23 10267

Figure A7. Nozzle Exit Plane Velocity Profiles  
Nozzle B



GP23-5785-13

Figure A8. Turbulence Intensity and Velocity Profiles  
Nozzle B  $z/D_B = 1.0$   $NPR = 1.10$

The free jet entrainment induced radial velocities were recorded by traversing the HFA probe in the axial ( $z/D$ ) direction at several radial ( $r/D$ ) stations. Figure A9 depicts the test hardware installation used to measure the induced velocities for nozzle A. Data points, recorded with the air off at the beginning and end of each axial traverse were summed and averaged to provide a correction factor to account for any extraneous drafts in the test cell. This average air off velocity (usually on the order of .03 m/sec) was subtracted from each of the measured induced velocities recorded during the traverse to yield a corrected entrainment velocity. Table A1 defines the axial and radial stations at which the entrainment velocities were recorded. Due to the larger diameter of nozzle B and the fixed HFA probe length, surveys of the nozzle B configurations were limited to  $z/D_B < 6$ .

In a check of the symmetry of the entrainment flow about the jet, it was discovered that the entrainment velocities measured at an azimuthal station of  $\phi = 0^\circ$  (see Figure A10) were generally lower and more unsteady than those measured at  $\phi = 180^\circ$ . Additional measurements made at  $\phi = 270^\circ$  produced results generally falling between those obtained at  $\phi = 0^\circ$  and  $\phi = 180^\circ$ . This flow asymmetry was found to persist for all nozzle configurations and all nozzle pressure ratios. In addition, rotating the nozzle  $180^\circ$  on the plenum produced no change in the azimuthal distribution of the asymmetry. It was thus concluded that the flow asymmetry was a result of the test cell structure and internal aerodynamics. Consequently, measurements of the entrainment velocities were recorded at azimuthal stations of  $\phi = 0^\circ$ ,  $180^\circ$  and  $270^\circ$  for each configuration to provide a larger, more representative data base. (Hardware restrictions prevented surveys at the  $\phi = 90^\circ$  location.)

**A.2.3 Test Results** - The data reduction technique described in Section A.2.1 was utilized in conjunction with a potential core length,  $z_c$ , of  $6D$  to calculate  $m_1$  and  $m_2$ . (A sensitivity study indicated  $m_1$  and  $m_2$  relatively independent of  $z_c$  for  $4 \leq z_c/D \leq 8$ .) The calculated values of  $m_1$  and  $m_2$  determined for nozzle A are presented in Figure A11 as a function of NPR. Also shown in the figure is the value of  $m_1$  determined for nozzle B in the baseline TO configuration at NPR = 1.10. As seen in the figure both entrainment rates  $m_1$  and  $m_2$  are higher than the values determined by Kleis and Foss which are currently used in the MCAIR V/STOL methodology.

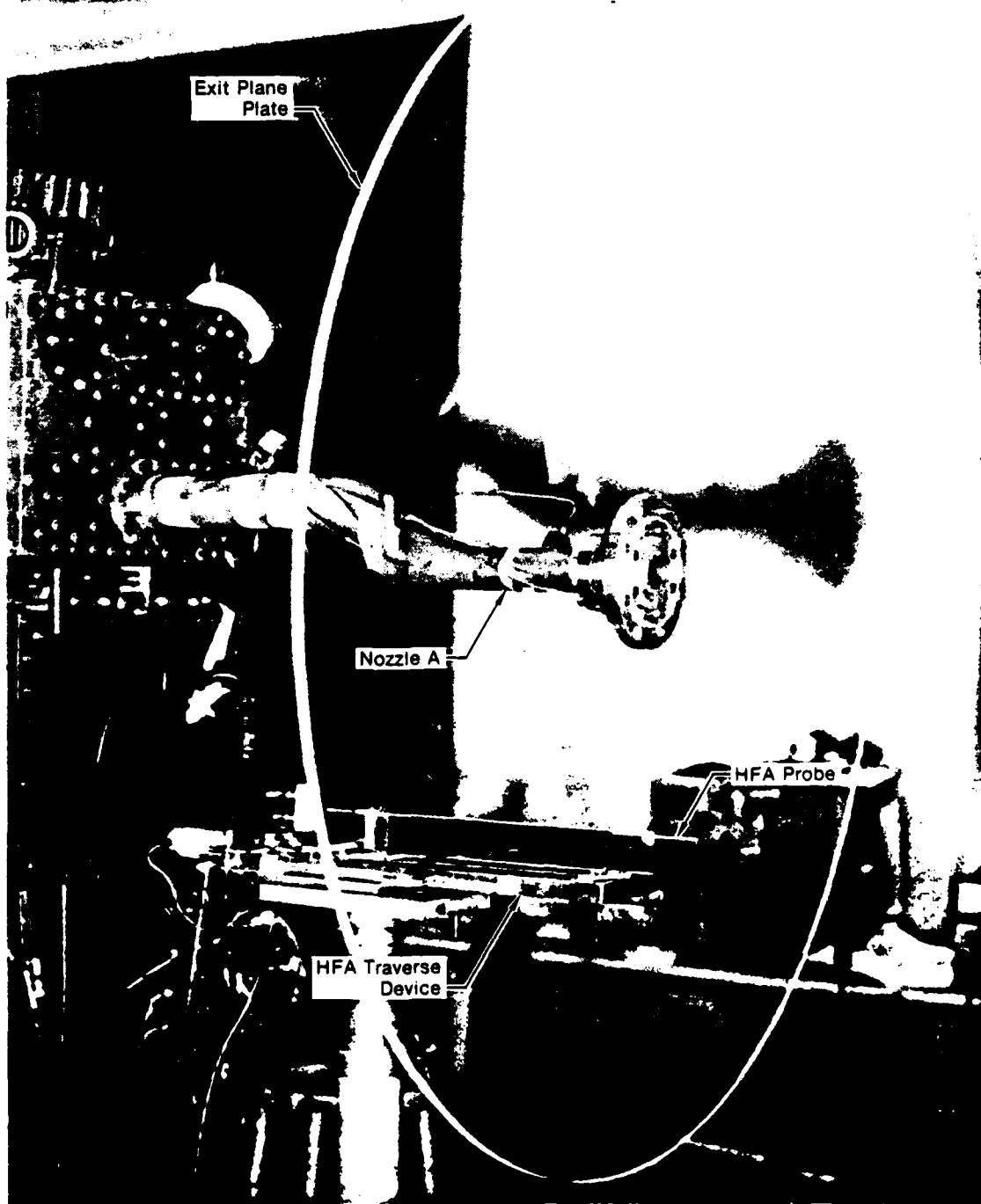


Figure A9. Induced Velocity Measurement Test Hardware  
Nozzle A



View Looking Upstream

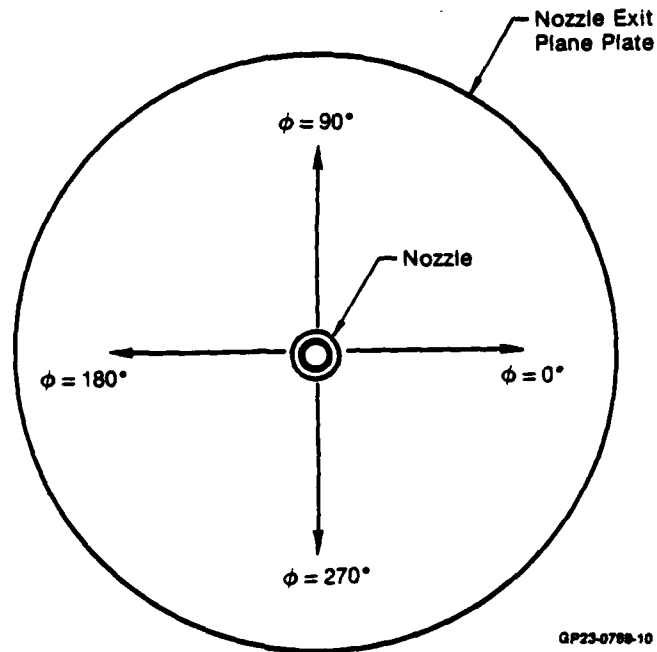


Figure A10. Probe Azimuthal Locations

Since the entrainment measurements for the turbulence effects investigation using nozzle B were limited to  $z/D \leq 6$ , it was not possible to measure  $m_2$  directly. Thus, based on the data of Kleis and Foss,  $m_2$  was defined as

$$m_2 = \frac{m_1}{.66} \quad (A4)$$

The effect of the magnitude of  $m_2$  on the calculation of  $m_1$  was investigated and found to be relatively insignificant. Figure A12 presents the effect of turbulence intensity on  $m_1$  for  $NPR = 1.10$ . The turbulence intensity shown is the value at the jet centerline at  $z/D = 1.0$ . As seen from the figure, there seems to be little correlation between  $u'/\bar{U}$  and  $m_1$ . However, it is noteworthy that  $m_1$  is again higher than the value determined by Kleis and Foss for all four cases.

The mass entrainment induced by jets issuing from both nozzle A and nozzle B at  $NPR = 1.10$  was also calculated under IRAD funding using the direct method of integrating the free jet velocity profiles. The velocity profiles were obtained during the free jet surveys using the hot film anemometer. Figure A13 compares the mass entrainments determined using both the indirect and direct methods for nozzle A and nozzle B. The agreement between the two methods is seen to be good, particularly in the potential core region. Also shown in the figure for comparison is the mass entrainment determined by Kleis and Foss.

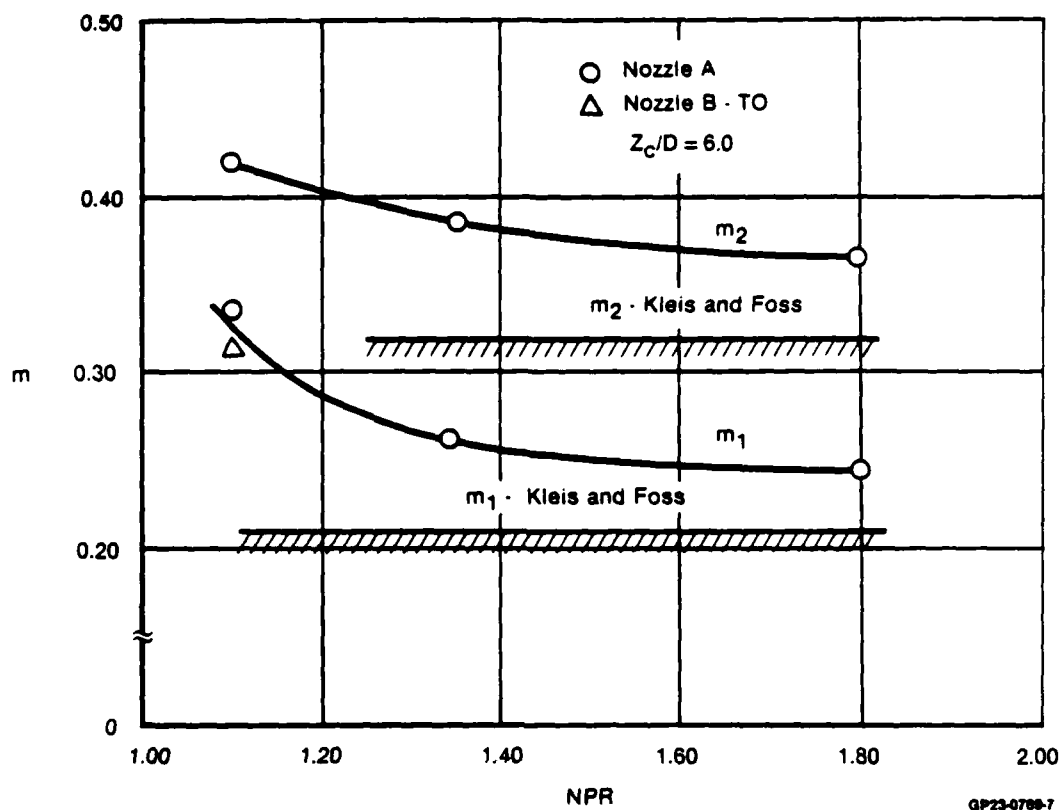


Figure A11. Effect of Nozzle Pressure Ratio on Free-Jet Entrainment

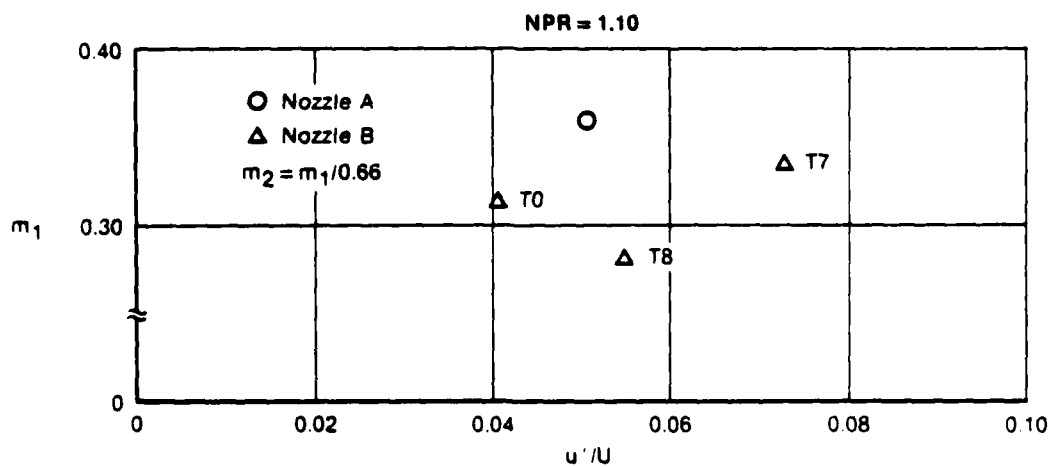


Figure A12. Effect of Turbulence Intensity on  $m_1$

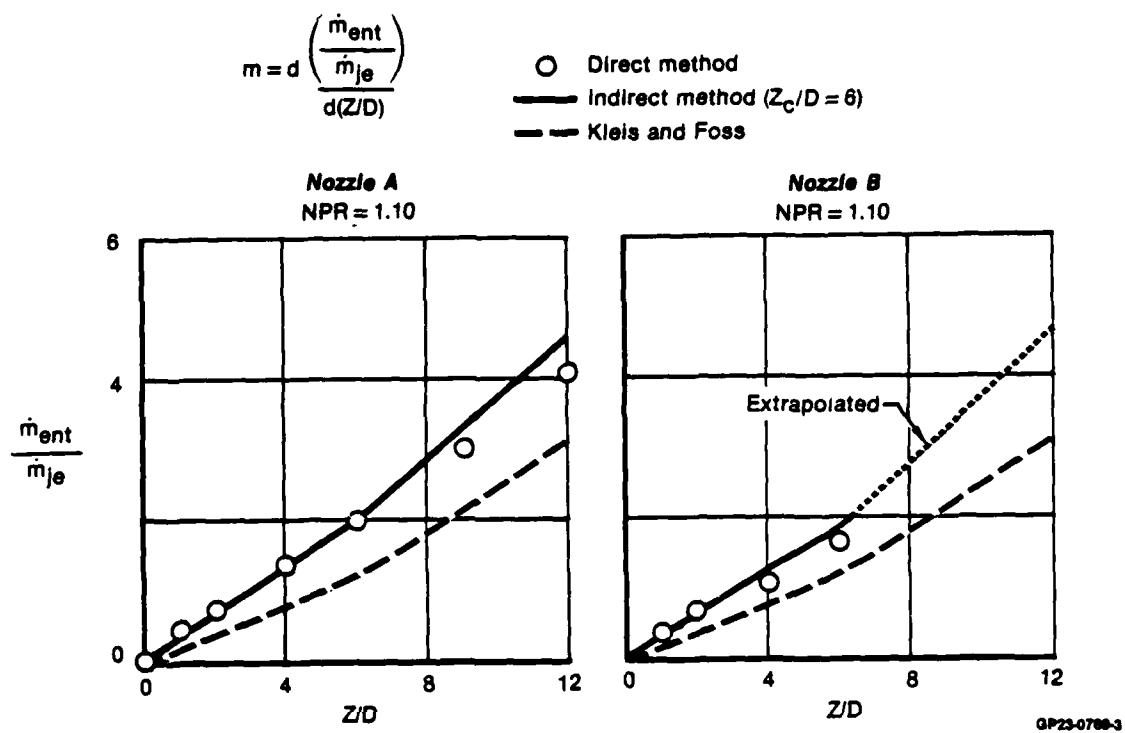


Figure A13. Comparison of Indirect and Direct Methods for Determining Free-Jet Entrainment

NADC-81106-60  
DISTRIBUTION LIST

	<u>No. of Copies</u>
NAVAIR . . . . .	2
(1 for AIR-311D)	
(1 for AIR-5301)	
CONAVAIRPROPCEN, Trenton, NJ. . . . .	1
DTNSRDC, Bethesda, MD . . . . .	1
(1 for Dr. H. Chaplin)	
CNR, Arlington, VA . . . . .	1
(1 for Dr. R. Whitehead)	
NAVPGSCOL, Monterey, CA . . . . .	1
(1 for Dr. N. Platzer)	
NASA, Ames, Moffett Field, CA . . . . .	2
(1 for D. Koenig)	
(1 for D. Hickey)	
NASA, Langley, Hampton, VA . . . . .	1
(1 for R. Margason)	
NASA, Lewis, Cleveland, OH . . . . .	1
AFWAL/FS, WPAFB, OH . . . . .	1
AFWAL/FIMM, WPAFB, OH . . . . .	1
(1 for C. Jobe)	
ASD, WPAFB, OH . . . . .	1
NAVAIRDEVCEEN, Warminster, PA . . . . .	23
(1 for 605)	
(2 for 60011)	
(3 for 8131)	
(17 for 6053)	
CG, Army Aviation Systems Command, St. Louis, MO . . . . .	1
DTIC . . . . .	12

Continued on Inside of Cover

DISTRIBUTION LIST

	<u>No. of Copies</u>
Analytical Methods, Inc., Redmond, WA 98052 . . . . . (1 for B. Maskew)	1
Boeing Company, Seattle, WA 98101 . . . . . (1 for E. Omar)	1
Calspan, Buffalo, NY 14221 . . . . .	1
Computational Mechanics, Inc., Knoxville, TN 37920 . . . . . (1 for J. Baker)	1
Fairchild Republic Corporation, Farmingdale, L.I., NY 11735 . . . .	1
General Dynamics Corporation, Ft. Worth, TX 76108 . . . . . (1 for C. Smith) (1 for W. Folley)	2
Grumman Aerospace Corporation, Bethpage, L.I., NY 11714 . . . . . (1 for S. Kalamaris)	1
Lockheed-California Company, Burbank, CA 91503 . . . . . (1 for A. Yackle) (1 for L. Miranda)	2
Lockheed-Georgia Company, Marietta, GA 30063 . . . . .	1
McDonnell Douglas Corporation, Long Beach, CA 90808 . . . . . (1 for P. Henne)	1
Nielson Engineering & Research, Inc., Mountain View, CA 94043 . . . . (1 for S. Spangler) (1 for M. Mendenhall)	2
Northrup Corporation, Hawthorne, CA 90250 . . . . . (1 for P. Wooler) (1 for B. Hunt)	2
Rockwell International, Columbus, OH 43216. . . . . (1 for J. Dehart) (1 for W. Palmer)	2
Rockwell International, Los Angeles, CA 90009 . . . . . (1 for A. Schoenhert)	1
Vought Corporation, Dallas, TX 75222 . . . . . (1 for T. Beatty) (1 for H. Sherrieb)	2

**DAT  
ILM**